Faculty of Natural Science and Technology
Department of Physics

NTNU
Innovation and Creativity

MASTER'S THESIS FOR

STUD. TECHN. HENRIK ENOKSEN

Thesis started:	20.01.2009
Thesis submitted:	16.06.2009

DISCIPLINE: THEORETICAL PHYSICS

Norsk tittel: *"Teoretiske og numeriske studier av spredning av polarisert lys på en relakserende periodisk nanostrukturert høyviskøs fluidoverflate"*

English title: *"Theoretical and Numerical Studies of Diffractive Scattering of Polarized Light from a Relaxing Periodic Nanostructured Highly Viscous Fluid Surface"*

This work has been carried out at the Department of Physics, Faculty of Natural Science and Technology, under the supervision of professor Ingve Simonsen.

Trondheim, 16.06.2009

Ingve Simonsen

Responsible supervisor

Professor at Department of Physics

Abstract

This thesis is written with the main purpose of finding a new indirect method for determining the temperature dependent viscosity of a material. The method is to compare intensities of reflected diffraction orders during surface relaxation, obtained by experiment, where the temperature is known, and by simulation, where the viscosity is known. Data inversion will then yield the temperature dependent viscosity.

The relaxation dynamics is derived within the small slope approximation which yields relaxation times linear in the viscosity. As it turns out, we only need one simulation due to this linear dependency. We then study scattering of polarized light from a periodic nanostructured surface, which relaxes in time according to the relaxation dynamics.

Rigorous scattering simulations are carried out, confronted with theory and compared to preliminary experimental data. The qualitative behavior of our simulation results corresponds well with experimental results. It is found that the method shows promising results.

Sammendrag

Målet med denne oppgaven er å finne en ny indirekte måte å måle et materials temperaturavhengige viskositet på. Metoden går ut på å måle intensiteten i forskjellige diffraksjonsordre over tid mens overflaten relakserer, både eksperimentelt, hvor temperaturen er kjent, og gjennom simuleringer, hvor viskositeten er kjent. Deretter inverterer vi intensitetsdataene for å få viskositet som funksjon av temperatur.

Dynamikken bak relakseringen er utledet ved å anta at overflaten er glatt, noe som gir linear avhengighet mellom relakseringstid og viskositet. Dette gjør at vi kun trenger én simulering for å finne den temperaturavhengige viskositeten. Deretter studerer vi spredning av polarisert lys fra en nanostrukturert overflate som relakserer i tid i henhold til relakseringsdynamikken.

Vi gjør rigorøse spredningssimuleringer som blir satt opp mot teori og deretter sammenlignet med innledende eksperimentelle resultater. Den kvalitative oppførselen til simuleringene stemmer godt overens med eksperimentelle resultater. Sammenligningene viser at metoden virker lovende.

Preface

This thesis is the result of the course TFY4900 Physics, Master's Thesis. The duration of the course was one semester with a suggested workload of 48 hours per week.

I have worked with electromagnetic scattering from a relaxing surface with a goal to find a way to indirectly measure the temperature dependent viscosity of a material. The experimentalists in Paris had problems with their experimental setup and therefore could not provide me with the experimental data I needed to reach my goal. Nevertheless, I have investigated several aspects of this surface scattering which might help the experimentalists make better decisions when designing the experimental setup.

I have learned a lot by working on this thesis. At first I had to learn myself Fortran90, which I had never touched upon before. Then I had to delve into electromagnetic theory and how to solve scattering problems numerically. Finally I had to combine the scattering with the hydrodynamical model I derived in my specialization project last semester. It has been interesting and rewarding. All in all, I am happy with the final result.

Acknowledgments

First, I would like to thank my supervisor, professor Ingve Simonsen, for invaluable guidance during the course of this Master's thesis. Without his help, the programming and implementation of the scattering program would have been very difficult. Also, his ability to motivate and support a horde of master students at once is impressive.

The French guys, Etienne Barthel and Jeremie Teisseire, also deserve a big thank. The preliminary experimental data they provided made it much easier to discuss my results. Also thank you for the photos.

I want to thank all my fellow students for five years of great fun. I have to give a special thank to Øivind Syversen for constantly providing me with coffee and Halvor Lund for his useful feedback and excellent proofreading.

Finally, I have to thank my girlfriend, Sigrid Grepstad, for her love, motivation and our wonderful Skype-dates. We made it!

Trondheim, 15th June 2009
Henrik Enoksen

Contents

Chapter 1

Introduction

Nanoimprint lithography is a method of making nanostructured surfaces, usually in thin polymer films. It was first invented by S. Chou *et al.* [1] in 1995. Several variations and implementations have since been developed.

Chou's method is elegant in its simplicity. The polymer film is heated to a temperature above its *glass transition temperature*, T_g, while a mold, with a predefined pattern, is pressed into the film. The glass transition temperature is the temperature where an amorphous solid, like a polymer, becomes soft on heating. When the polymer has filled the depressions of the mold, a cooling process is initiated. After cooling the polymer down to a temperature below T_g, the mold is removed and the nanostructured polymer film is ready for use. Figure 1.1 illustrates the process. The polymer films are usually prepared by spin coating [3]. This is a simple method where a solution is placed on a substrate which then is rotated at high speed to obtain the desired thickness, see figure 1.2. This is caused by centrifugal forces that spread the solution over the substrate. The higher the speed, the thinner the film.

Devices made with nanolithography imprinting are used in electrical, optical and biological applications. Examples include MOSFET transistors, polarizers, anti-reflective structures and biomolecular sorting devices.

There are still challenges with this method. For instance, how are the depressions in the mold filled by the polymer? An array of narrow depressions is more quickly filled

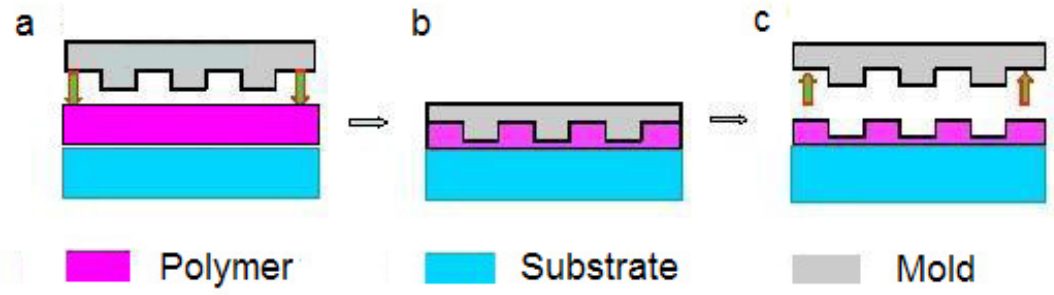

Figure 1.1: Illustration of the imprinting process. **a**: The mold is pressed into the polymer film of temperature $T > T_g$. **b**: The polymer fills the depressions of the mold. **c**: The mold is removed after cooling the polymer to a temperature $T < T_g$. Figure is inspired by Reference [2].

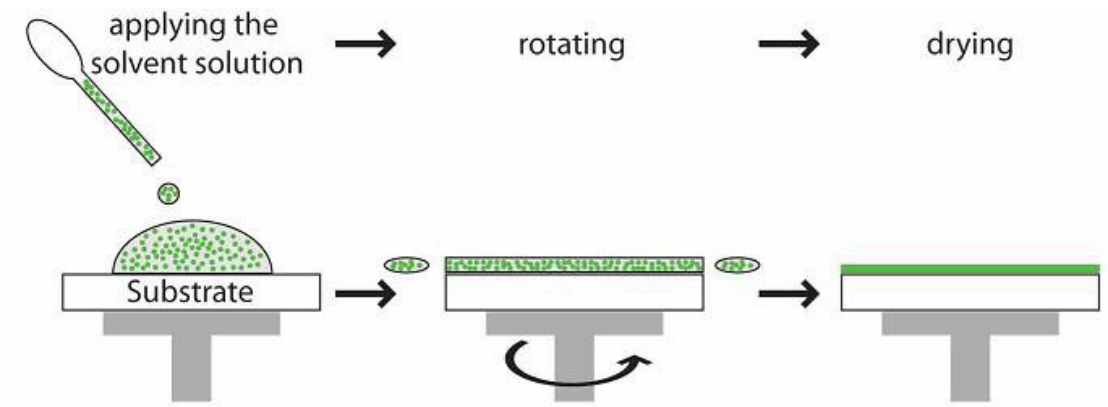

Figure 1.2: Illustration of the principle behind spin coating. Centrifugal forces push the solution outwards during the rotation. The figure is taken from Reference [2].

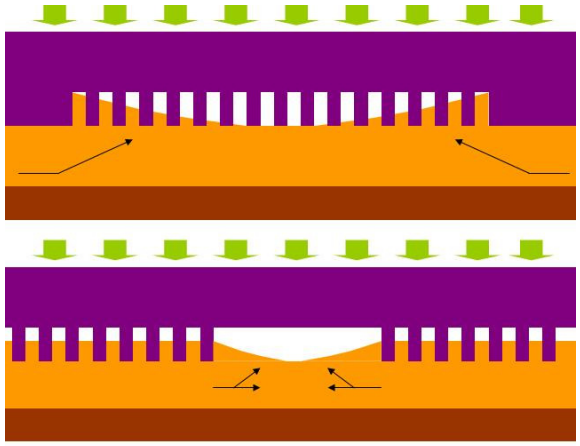

Figure 1.3: Illustration of imprinting problems. Top: An array of thin depressions is more quickly filled on the edges than in the center. Bottom: Wide depressions tend to fill slower than thin depressions. The figure is taken from Reference [4].

on the edges than in the center. Wide depressions tend to be filled slower than narrow depressions. This is illustrated in figure 1.3. Both of these problems may result in inaccurate imprinting.

For industrial purposes, time- and cost efficient large scale manufacturing is of great interest. Gravitational effects prevail when the mold gets large, which may result in uneven imprinting. How long should the cooling process go on before the polymer film is solid and the mold can be removed without destroying the structured film?

The temperature-dependent viscosity of the polymer is the interesting material parameter for this problem. Near the glass transition temperature, the viscosity changes rapidly, see figure 1.4. By knowing the temperature dependence, a manufacturer knows exactly at which temperature it is safe to remove the mold, thus making the manufacturing process more efficient and profitable.

Unfortunately, it is hard to measure the viscosity directly. Therefore, with the aim of an indirect way of determining this quantity, an optical diffraction experiment was designed and conducted to measure the intensities of the various diffraction orders during the time period of relaxation after heating. The idea is to compare the experimental

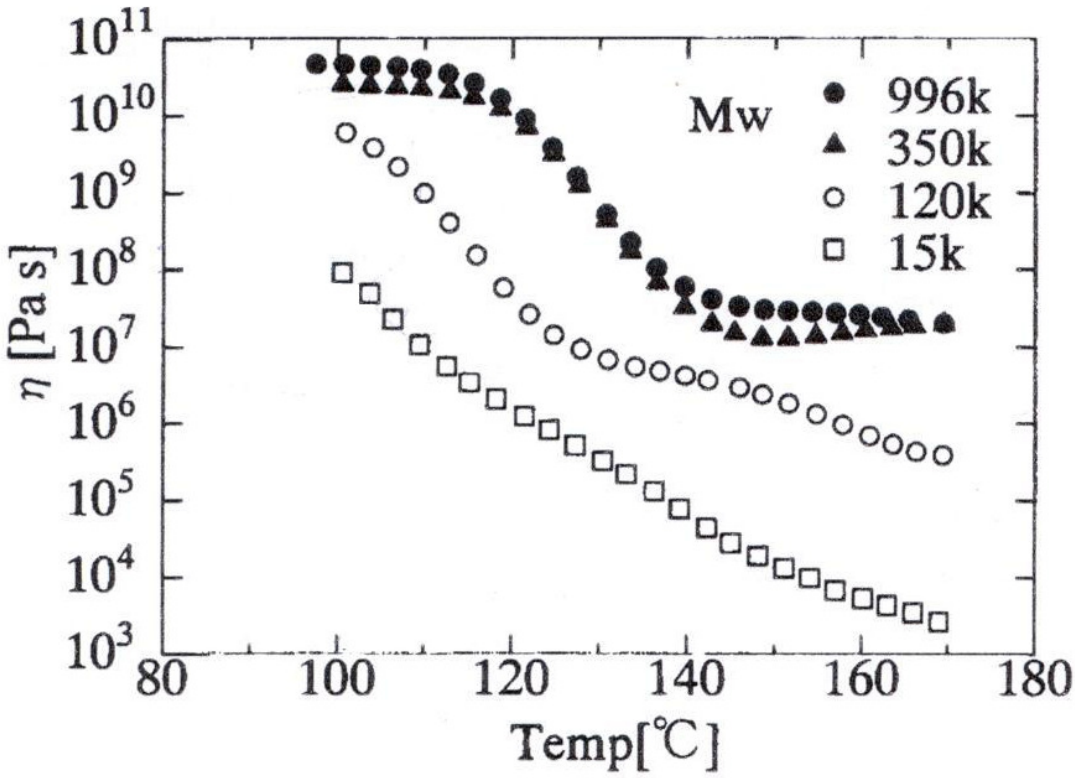

Figure 1.4: Viscosity, η, as function of temperature for PMMA of different molecular weights, M_w in g/mol. The glass transition is seen as the sudden change in viscosity for the two heaviest polymers. The two lighter polymers have T_g below 100°C. The graph is taken from Reference [5].

results with a hydrodynamical model to find viscosity as a function of temperature, $\eta(T)$. This experiment was designed by a group of experimentalists at Saint-Gobain Recherche, Paris. They have provided all experimental data used in this thesis. We have done scattering simulations, theoretical contemplations and developed a hydrodynamical model for the relaxation.

This hydrodynamical model was found in the specialization project. It is simple but yields good qualitative results. Most of the theory behind and the derivation of this model is included in this thesis to give the reader a complete description of the method.

The main focus of this thesis has been the scattering of light from the relaxing surface. We use the simple hydrodynamical model to simulate the relaxation, while a rigorous numerical method is used to solve the scattering problem. Unfortunately, there were problems with the experimental setup which caused delays. Therefore, we did not get enough experimental data to find $\eta(T)$ in time. Nevertheless, we compare our simulation results with preliminary experimental results. We also investigate the importance of different aspects of the experiment from a theoretical point of view, such as polarization and mismatch between the dielectric functions of the different layers of the experimental samples. The material we investigate is the polymer Poly-methyl methacrylate (PMMA).

This thesis is organized as follows: In chapters 2 and 3, we outline fundamental electromagnetic theory and surface scattering. The content of these two chapters is used in chapter 4 to derive a rigorous numerical method for solving the surface scattering problem. Chapters 5 and 6 present fundamental hydrodynamics and the derivation of a simple model for how periodic nanostructured highly viscous fluid surfaces relax. In chapter 7 we explain how we combine the hydrodynamical model with the rigorous numerical method to solve the scattering from a relaxing surface. We also present how we can do the optical diffraction experiment and how we compare the simulation results with the experimental data to obtain the viscosity as a function of temperature. In chapter 8, we present our results which are discussed in chapter 9 where future work is also presented. Finally, we summarize and conclude in chapter 10.

Chapter 2

Electromagnetism

In this section we will outline the basic electromagnetic equations which explain electromagnetic waves and their behavior at interfaces. We will also briefly explain polarization and the energy carried by the electromagnetic waves. Lastly, we will introduce the grating equation which describes how electromagnetic waves behave when they are scattered of a structured surface with period close to the wavelength of the waves.

2.1 Maxwell's equations

All of electromagnetism is contained within four equations called Maxwell's equations. These are [6]

$$\nabla \cdot \mathbf{E} = \frac{\rho}{\epsilon_0} \,, \tag{2.1a}$$

$$\nabla \cdot \mathbf{B} = 0 \,, \tag{2.1b}$$

$$\nabla \times \mathbf{E} = -\frac{\partial \mathbf{B}}{\partial t} \,, \tag{2.1c}$$

$$\nabla \times \mathbf{B} = \mu_0 \mathbf{J} + \mu_0 \epsilon_0 \frac{\partial \mathbf{E}}{\partial t} \,. \tag{2.1d}$$

Here, $\mathbf{E}$ and $\mathbf{B}$ are the electric and magnetic field vectors. Bold symbols denote vectors and $\cdot$ denotes a scalar product. The electromagnetic field in vacuum consists of these two vectors. The constants ϵ_0 and μ_0 are the permittivity and permeability in vacuum, respectively. Moreover, ρ and $\mathbf{J}$ denote the charge density and current density, respectively. Equations (2.1) only apply to point charges in vacuum. To investigate large collections of point charges, like dielectrics and metals, we have to introduce effective fields. These are the electric displacement field $\mathbf{D}$ and the $\mathbf{H}$-field[1] defined via [6]

$$\mathbf{D} = \epsilon \mathbf{E} \,, \tag{2.2a}$$

$$\mathbf{B} = \mu \mathbf{H} \,, \tag{2.2b}$$

where $\epsilon = \epsilon_r \epsilon_0$ denotes the permittivity of the medium and $\mu = \mu_r \mu_0$ denotes the permeability of the medium. The dimensionless quantities ϵ_r and μ_r are the relative permittivity and permeability which are 2nd order tensors depending on the spatial

[1] This field is often called the magnetic field, but as $\mathbf{B}$ is the fundamental quantity, we will call it just $\mathbf{H}$. [7]

variable $\mathbf{x}$, the field vectors $\mathbf{E}$ and $\mathbf{H}$ and the frequency, ω, of the field. However, when the medium in question is isotropic and homogeneous, these tensors reduce to scalars. Furthermore, if the field strengths are not too large, they can be treated as independent of the field vectors. In this case, we are dealing with linear electromagnetic theory which simplifies our problem significantly.

The permittivity is of great interest as it determines how the medium reacts to electromagnetic fields. It is often called the dielectric function, which we will call it from now. The dielectric function is a complex function where the real part is connected to reflection and refraction of electromagnetic waves, while the imaginary part is connected to the absorption of electromagnetic energy in the medium. The refractive index, n_1, of a medium is the real part of the square root of the relative permittivity, $\sqrt{\epsilon_r} = n_1 + in_2$.

Finally, $\mathbf{D}$ and $\mathbf{H}$ are the effective fields which describe the effect of electromagnetic fields in matter. Replacing the ϵ_0 and μ_0 in Maxwell's equations (2.1) with ϵ and μ and using equations (2.2), we obtain Maxwell's equations in matter [6]

$$\nabla \cdot \mathbf{D} = \rho \,, \tag{2.3a}$$

$$\nabla \cdot \mathbf{B} = 0 \,, \tag{2.3b}$$

$$\nabla \times \mathbf{E} = -\frac{\partial \mathbf{B}}{\partial t} \,, \tag{2.3c}$$

$$\nabla \times \mathbf{H} = \frac{\partial \mathbf{D}}{\partial t} + \mathbf{J} \,. \tag{2.3d}$$

The charge density ρ and the current density $\mathbf{J}$ act as sources for the electromagnetic field in matter, $\mathbf{E}$ and $\mathbf{H}$, and they fulfill the *continuity equation*

$$\frac{\partial \rho}{\partial t} + \nabla \cdot \mathbf{J} = 0 \,. \tag{2.4}$$

2.2 Electromagnetic waves

We will now derive the wave equation for the electric field for the system most relevant to this thesis, namely an isotropic, homogeneous and source-free medium ($\rho = 0$ and $\mathbf{J} = 0$). The dielectric function of a homogeneous medium is independent of $\mathbf{x}$, and is thus spatially constant. Taking the curl of equation (2.3c) and inserting equations (2.3d) and (2.2) we obtain

$$\nabla \times (\nabla \times \mathbf{E}) + \mu\epsilon \frac{\partial^2 \mathbf{E}}{\partial t^2} = 0 \,. \tag{2.5}$$

Here, the electric field is dependent on both space and time, *i.e* $\mathbf{E} = \mathbf{E}(\mathbf{x}, t)$. By applying the vector identity $\nabla \times (\nabla \times \mathbf{A}) = \nabla(\nabla \cdot \mathbf{A}) - \nabla^2 \mathbf{A}$ and equation (2.3a), we end up with the wave equation for the electric field

$$\nabla^2 \mathbf{E} - \mu\epsilon \frac{\partial^2 \mathbf{E}}{\partial t^2} = 0 \,. \tag{2.6}$$

Solutions to this equation are known as *electromagnetic waves*. These solutions tend to have a harmonic time dependence $\exp(-i\omega t)$. Inserting this time-dependence into the wave equation (2.6) and using the relation $\mu_0\epsilon_0 = 1/c^2$, where c is the velocity of light, yields

$$\left(\nabla^2 + \mu_r \epsilon_r \frac{\omega^2}{c^2}\right) \mathbf{E} = 0 \,, \tag{2.7}$$

which is the *Helmholtz equation*. Here, the electric field is no longer time-dependent, *i.e.* $\mathbf{E} = \mathbf{E}(\mathbf{x}|\omega)$. The wave equation and its corresponding Helmholtz equation for $\mathbf{H}$ can be found in the same manner by eliminating the electric field.

To find the *dispersion relation* we insert a plane wave, $\mathbf{E} = \exp(i\mathbf{k}\cdot\mathbf{x})$ into Helmholtz equation (2.7) and obtain

$$\mathbf{k}\cdot\mathbf{k} - \epsilon_r\mu_r\frac{\omega^2}{c^2} = 0\,. \tag{2.8}$$

By splitting the scalar product into a parallel and a perpendicular part, q and $\alpha(q,\omega)$ respectively, and taking the square root of the resulting expression we get

$$\alpha(q,\omega) = \sqrt{\epsilon_r\mu_r\frac{\omega^2}{c^2} - q^2}\,. \tag{2.9}$$

By parallel and perpendicular part we mean parallel and perpendicular to the xy-plane.

Electromagnetic waves travel in the direction of the wave vector $\mathbf{k}$. When $\rho = \mathbf{J} = 0$ we get the condition $\mathbf{k}\cdot\mathbf{E} = 0$ from Gauss' law (2.3a) and $\mathbf{k}\cdot\mathbf{H} = 0$ from equation (2.3b) when we insert a plane wave. Furthermore, by utilizing the plane wave and integrating equation (2.3c) over time we get $\mathbf{H} \sim \mathbf{k}\times\mathbf{E}$. Hence, electromagnetic waves are transverse and the electric field and $\mathbf{H}$ are mutually perpendicular.

2.3 Polarization

The *polarization* of an electromagnetic field is determined by which field that is perpendicular to the *plane of incidence*. The plane of incidence is defined as the plane formed by the incident, reflected and transmitted wave vectors, see figure 2.1. There are two kinds of polarization, namely s- and p-polarization. In the first case, the electric field is perpendicular to the plane of incidence, while in the latter case, the electric field is parallel. The notation s comes from the German word *senkrecht* which means perpendicular while p comes from parallel.

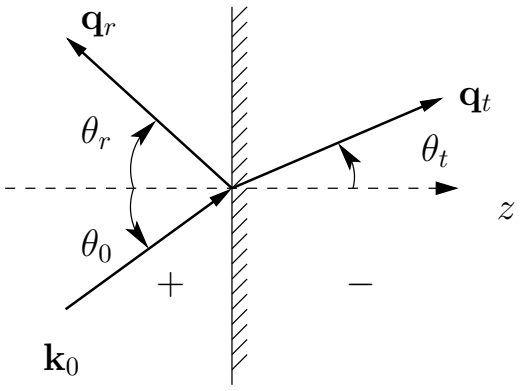

Figure 2.1: Illustration of a incoming electromagnetic wave with wave vector $\mathbf{k}_0$ being both reflected ($\mathbf{q}_r$) from and transmitted ($\mathbf{q}_t$) through an interface between two different media labeled $\pm$. The plane of incidence is the paper plane. θ_0 is the angle of incidence, θ_r is the angle of reflection and θ_t is the angle of refraction.

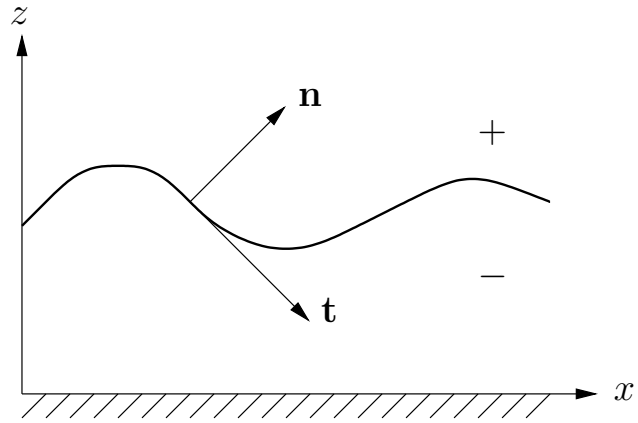

Figure 2.2: Interface between two media, labeled ±. **n** and **t** are the normal and tangential unit vectors to the interface.

2.4 Boundary conditions

Maxwell's equations can be solved in regions without boundaries, but boundaries do exist in the real world. Therefore it is useful to know how electromagnetic fields behave at interfaces between two different media. Consider the geometry shown in figure 2.2. It shows the interface between two isotropic, homogeneous and linear media labeled ±. **n** is a unit normal vector for the interface directed into medium +. The boundary conditions are then

$$\mathbf{n} \cdot (\mathbf{B}_- - \mathbf{B}_+) = 0 \,, \tag{2.10a}$$
$$\mathbf{n} \cdot (\mathbf{D}_- - \mathbf{D}_+) = \rho_s \,, \tag{2.10b}$$
$$\mathbf{n} \times (\mathbf{E}_- - \mathbf{E}_+) = 0 \,, \tag{2.10c}$$
$$\mathbf{n} \times (\mathbf{H}_- - \mathbf{H}_+) = \mathbf{J}_s \,, \tag{2.10d}$$

where the indicies ± refers to the media where the fields are evaluated. ρ_s and $\mathbf{J}_s$ are the surface charge density and the surface current density respectively. The derivation of these boundary conditions are found in nearly every book on electromagnetic theory. See *e.g.* Jackson [6].

We require that the electromagnetic field vanishes at $\mathbf{r} = \pm\infty$. If not, the energy density would be infinite, which is unphysical.

2.5 Energy

The flow of electromagnetic energy is described by *Poynting's vector* [6]

$$\mathbf{S} = \mathbf{E} \times \mathbf{H}^* \,. \tag{2.11}$$

It describes the energy transported by the electromagnetic field $(\mathbf{E}, \mathbf{H})$ per unit time and unit area, *i.e.* it is the energy flux density. More useful is the time-average of this quantity, due to experimental measurements. It is given by

$$\langle \mathbf{S} \rangle_t = \frac{1}{2} \mathbf{E} \times \mathbf{H}^* \,. \tag{2.12}$$

Specifically, the flow of energy per time through a surface of area $\mathbf{a}$, where $mathbfa$ is an area vector, is $\mathbf{S} \cdot \mathbf{a}$. From this we get the power (energy flux) passing through the xy-plane

$$P = \int dx \int dy \, \mathrm{Re}\langle \mathbf{S}_z \rangle_t \ , \tag{2.13}$$

where $\mathrm{Re}\langle \mathbf{S}_z \rangle_t$ denotes the time-averaged real part of the z-component of Poynting's vector (2.11). For an effective one-dimensional surface, *i.e.* where the surface is constant in y-direction, the y-integration is trivial. Therefore the power reduces to

$$P = L_y \int dx \, \mathrm{Re}\langle \mathbf{S}_z \rangle_t \ , \tag{2.14}$$

where L_y is the length of the surface in y-direction.

2.6 Fresnel's equations

Fresnel's equations give the amplitudes of the electromagnetic field for reflection from and transmission through a plane surface. Due to the boundary conditions (2.10), Fresnel's equations for s-polarized fields are different from those for p-polarized fields. The reflection amplitudes can be expressed as [8]

$$r_s = \frac{\cos\theta_0 - \sqrt{n^2 - \sin^2\theta_0}}{\cos\theta_0 + \sqrt{n^2 - \sin^2\theta_0}} \ , \tag{2.15a}$$

$$r_p = \frac{-n^2\cos\theta_0 + \sqrt{n^2 - \sin^2\theta_0}}{n^2\cos\theta_0 + \sqrt{n^2 - \sin^2\theta_0}} \ , \tag{2.15b}$$

where r_s and r_p are the reflection amplitudes for s- and p-polarized fields respectively, θ_0 is the angle of incidence and $n = \sqrt{\epsilon_-/\epsilon_+}$ is the ratio of the refractive indices of the two media. The corresponding amplitudes for transmission can be written as [8]

$$t_s = \frac{2\cos\theta_0}{\cos\theta_0 + \sqrt{n^2 - \sin^2\theta_0}} \ , \tag{2.16a}$$

$$t_p = \frac{2n\cos\theta_0}{n^2\cos\theta_0 + \sqrt{n^2 - \sin^2\theta_0}} \ . \tag{2.16b}$$

These amplitudes are the ratios of the reflected (transmitted) field and the incoming field. Squaring them yields the so-called reflectance and transmittance, R and T, respectively [7]

$$R_\nu = |r_\nu|^2 = \left| \frac{E_\nu^r}{E_\nu^i} \right|^2 \ , \tag{2.17a}$$

$$T_\nu = |t_\nu|^2 = \left| \frac{E_\nu^t}{E_\nu^i} \right|^2 \ . \tag{2.17b}$$

Here, the index ν denotes the polarization of the field. The square of the field is proportional to the value of Poynting's vector (2.11). Hence, the sum of R and T should be unity if there is no absorption

$$R + T = 1 \ . \tag{2.18}$$

We must assume that there is no absorption for this relation to hold. The interpretation of this relation is conservation of energy; the sum of reflected and transmitted energy is equal to the incoming energy.

From now on, the reflectances from plane surfaces will be called Fresnel reflectances and be denoted as R_ν^F, where ν denotes the polarization.

2.7 Diffraction and gratings

A beam impinging onto an interface between two materials may be reflected and/or transmitted depending on the properties of the materials and the beam. The dielectric functions of the materials determine the amount of energy that is reflected and transmitted. If the interface is periodic and the wavelength of the beam becomes comparable to the periodicity of the interface, diffraction effects arise. The *grating equation* tells us how many diffraction orders that appear and their location. Here, we will derive the grating equation for both reflection and transmission. We assume that the media are of some material of constant and real dielectric function. Furthermore, we only consider a one-dimensional interface, as this corresponds to our system.

We begin with considering a plane wave impinging onto a periodic surface. The boundary condition at the periodic surface implies that the incoming and reflected field must be joined with the transmitted field, *i.e.* $\mathbf{E}_0(\mathbf{x},t) + \mathbf{E}_r(\mathbf{x},t) = \mathbf{E}_t(\mathbf{x},t)$. It follows from this equality that

$$\mathcal{I}e^{i(\mathbf{k}_0\cdot\mathbf{x}-\omega t)} + \mathcal{R}e^{i(\mathbf{q}_r\cdot\mathbf{x}-\omega t)} = \mathcal{T}e^{i(\mathbf{q}_t\cdot\mathbf{x}-\omega t)} \,, \tag{2.19}$$

where $\mathcal{I}$, $\mathcal{R}$ and $\mathcal{T}$ are the amplitudes of the incoming, reflected and transmitted field respectively. These amplitudes are independent of the spatial variable $\mathbf{x}$. Since each of the fields come from the same source they have the same frequency. Hence, the time dependent part of the exponentials of equation (2.19) are equal. Boundary condition (2.19) has to hold for *all* $\mathbf{x}$ which implies

$$\mathbf{k}_0 \cdot \mathbf{x} = \mathbf{q}_r \cdot \mathbf{x} = \mathbf{q}_t \cdot \mathbf{x} \,. \tag{2.20}$$

To describe a periodic surface we need a set of *reciprocal vectors*, $\mathbf{G}$, which are the inverse periodicity of the surface. For a one-dimensional interface the reciprocal vector is [9]

$$\mathbf{G}_m = \frac{2\pi m}{L}\hat{\mathbf{x}} \,, \tag{2.21}$$

where L is the period of the interface, $\hat{\mathbf{x}}$ is the real-space unit vector and m is an integer.

The difference between the incoming wave vector and the outgoing wave vectors, $\mathbf{k}_0$ and $\mathbf{q}_{r/t}$ respectively, is called the scattering vector

$$\Delta\mathbf{q} = \mathbf{q}_{r/t} - \mathbf{k}_0 \,. \tag{2.22}$$

When the scattering vector differs significantly from the reciprocal vector, the amplitude of the scattered wave is negligibly small, see *e.g.* chapter 2 of Kittel [9]. Therefore, the diffraction orders appear at locations for which the scattering vector equals a reciprocal vector

$$\Delta\mathbf{q} = \mathbf{G}_m \tag{2.23}$$

for some m.

At the surface, the lateral components of the wave vectors should be conserved. These are of the form $k_{||} = \sqrt{\epsilon}\frac{\omega}{c}\sin\theta$. Looking at the parallel components of (2.23), where $\Delta\mathbf{q} = \mathbf{q}_r - \mathbf{k}_0$, yields for reflection

$$\sqrt{\epsilon_+}\frac{\omega}{c}\sin\theta_r^{(m)} - \sqrt{\epsilon_+}\frac{\omega}{c}\sin\theta_0 = \frac{2\pi m}{L}\ , \tag{2.24}$$

where θ_0 is the angle of incidence and $\theta_r^{(m)}$ is the reflection angle of diffraction order m. Using $\omega = 2\pi c/\lambda$, where λ is the wavelength of the incident electromagnetic wave, with equation (2.24) yields the reflection grating equation

$$\sin\theta_r^{(m)} - \sin\theta_0 = \frac{m\lambda}{\sqrt{\epsilon_+}L}\ . \tag{2.25}$$

Doing the same for the scattering vector with transmission instead of reflection yields the transmission grating equation

$$\sqrt{\epsilon_-}\sin\theta_t^{(m)} - \sqrt{\epsilon_+}\sin\theta_0 = \frac{2\pi m}{L}\ . \tag{2.26}$$

Chapter 3

Surface scattering

In this section we will introduce a general geometry and derive the behavior of the scattered fields. Furthermore, we introduce the concept of the mean differential reflection coefficient which is a quantity related to experimental measurements. The last section outlines multilayer thin film scattering where transmitted light is reflected from several interfaces in a stack of thin films.

3.1 Scattering geometry

The surfaces we treat in this thesis are effectively one-dimensional as the surface profile function has a non-trivial dependence only on x, and because they are constant along the y–direction. The region above the surface is assumed to be air ($\epsilon_+(\omega) = 1$) and the one below consists of an isotropic, homogeneous dielectric medium characterized by a frequency-dependent dielectric function ($\epsilon_-(\omega) = \epsilon(\omega)$). Furthermore, we assume that the material is non-magnetic ($\mu_r = 1$) and that it is source-free ($\rho = 0$ and $\mathbf{J} = 0$). The geometry is shown in figure 3.1.

3.2 The scattered field

By assuming that the plane of incidence is the xz-plane and that the incident beam is either s- or p-polarized, one field component is sufficient to fully describe the electromagnetic field. This reduces the problem of determining the field from a vector problem to a scalar one. The primary field can thus be written as [10]

$$\Phi_\nu(x, z|\omega) = \begin{cases} H_y(x, z|\omega) \,, & \nu = p \,, \\ E_y(x, z|\omega) \,, & \nu = s \,. \end{cases} \tag{3.1}$$

We have suppressed the harmonic time-dependence to simplify the notation. Using equation (2.3c) and (2.3d) together with (2.2) we can calculate the remaining components from (3.1). For a p-polarized field, the components are

$$E_x = -\frac{i}{\omega\epsilon(\omega)} \frac{\partial}{\partial z} H_y(x, z|\omega) \,, \tag{3.2a}$$

$$E_z = \frac{i}{\omega\epsilon(\omega)} \frac{\partial}{\partial x} H_y(x, z|\omega) \,, \tag{3.2b}$$

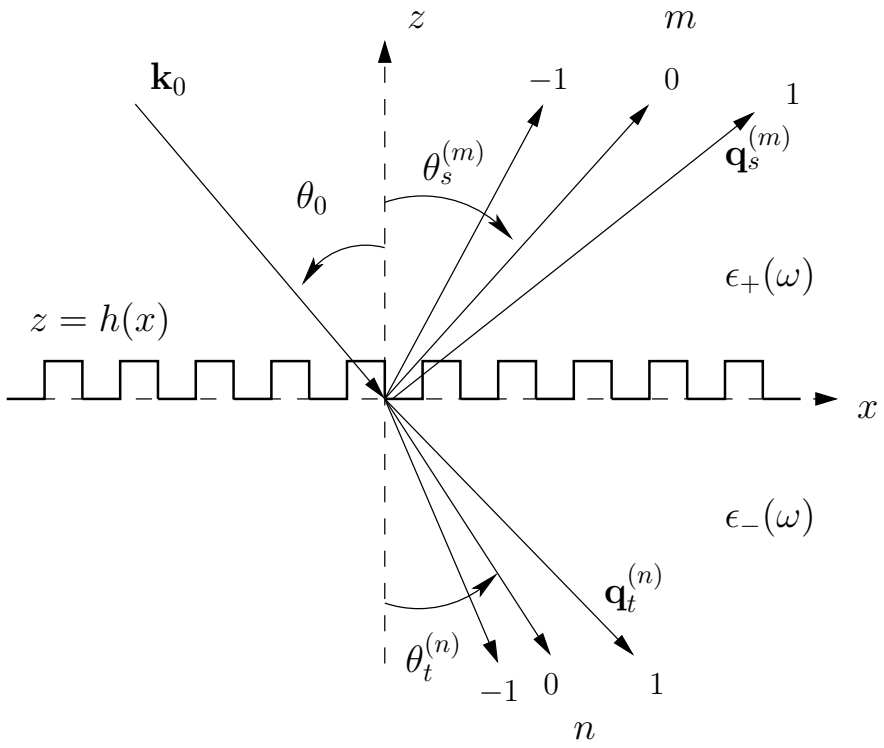

Figure 3.1: Illustration of a general one-dimensional scattering geometry. The surface is defined by $z = h(x)$ where the region above is assumed to be air ($\epsilon_+(\omega) = 1$), while the one below is a dielectric with a frequency-dependent dielectric function $\epsilon_-(\omega) = \epsilon(\omega)$. $\theta_s^{(m)}$ is the angle of diffraction order m for a reflected wave, while $\theta_t^{(n)}$ is the angle of diffraction order n for a transmitted wave. The positive direction of the angles are defined by the arrows. $\mathbf{k}_0$ is the wave vector of the incident beam with angle of incidence θ_0, while $\mathbf{q}_t^{(n)}$ and $\mathbf{q}_s^{(m)}$ are the transmitted and reflected, respectively, wave vectors.

and for an s-polarized field

$$H_x = \frac{i}{\omega\mu(\omega)} \frac{\partial}{\partial z} E_y(x, z|\omega) \ , \tag{3.3a}$$

$$H_z = -\frac{i}{\omega\mu(\omega)} \frac{\partial}{\partial x} E_y(x, z|\omega) \ . \tag{3.3b}$$

Here, $\epsilon(\omega)$ and $\mu(\omega)$ are dependent on the medium where the fields are evaluated.

3.2.1 Boundary conditions

The primary field $\Phi_\nu(x, z|\omega)$ is tangential to the surface for both polarizations. This way, boundary conditions (2.10a) and (2.10b) yield

$$\Phi_\nu^+(x, z|\omega)\,\big|_{z=h(x)} = \Phi_\nu^-(x, z|\omega)\,\big|_{z=h(x)} \ , \tag{3.4}$$

where $h(x)$ denotes the interface between air and the dielectric.

In order to satisfy the remaining boundary conditions we assume for simplicity that the surface $h(x)$ is a single-valued function of x. By single-valued, we mean that $h(x)$

has only one value for each x. Then, the unit normal vector of the surface $\mathbf{n}$ can be expressed as [11]

$$\mathbf{n} = \frac{(-h'(x), 0, 1)}{\sqrt{1 + (h'(x))^2}} , \tag{3.5}$$

where $h'(x)$ denotes the surface differentiated with respect to x. The normal derivative of the surface ∂_n is

$$\partial_n = \mathbf{n} \cdot \nabla = \frac{-h'(x)\partial_x + \partial_z}{\sqrt{1 + (h'(x))^2}} , \tag{3.6}$$

where ∂_i denotes a partial derivative with respect to spatial coordinate $i = x, z$.

Using the normal vector and its derivative we obtain the last boundary conditions for the primary field at the surface

$$\frac{1}{\kappa_\nu^+(\omega)} \partial_n \Phi_\nu^+(x, z|\omega) \big|_{z=h(x)} = \frac{1}{\kappa_\nu^-(\omega)} \partial_n \Phi_\nu^-(x, z|\omega) \big|_{z=h(x)} , \tag{3.7}$$

where $\kappa_\nu^\pm$ are defined as

$$\kappa_\nu^\pm = \begin{cases} \epsilon_\pm(\omega) , & \nu = p \\ \mu_\pm(\omega) , & \nu = s \end{cases} . \tag{3.8}$$

3.2.2 Asymptotic, far-field behavior of the scattered fields

Intensity measurements are in our case done far from the surface. Knowledge of the asymptotic far-field behavior of the scattered fields is thus essential. The fields have to satisfy the Maxwell's equations (2.3) and the boundary conditions at infinity. When we consider the scattering geometry depicted in figure 3.1, Maxwell's equations (2.3) are equivalent to the scalar version of the Helmholtz equation (2.7) of our primary field (3.1). Here, we find the asymptotic far-field behavior of $\Phi_\nu(x, z|\omega)$.

If the incoming field is a plane wave, it can be written as

$$\Phi_\nu^{inc}(x, z|\omega) = e^{ikx - i\alpha_0(k,\omega)z} , \tag{3.9}$$

where $\alpha_0(k, \omega)$ is the wave number in z-direction defined as (from equation (2.9))

$$\alpha_0(k, \omega) = \begin{cases} \sqrt{\frac{\omega^2}{c^2} - k^2} , & |k| < \frac{\omega}{c} , \\ i\sqrt{k^2 - \frac{\omega^2}{c^2}} , & |k| > \frac{\omega}{c} . \end{cases} \tag{3.10}$$

Here, we have put $\epsilon_r \mu_r = 1$ since the incoming field is located in air. Then the field in the region $z > \max h(x)$ can be written as [10]

$$\Phi_\nu^+(x, z|\omega) = \Phi_\nu^{inc}(x, z|\omega) + \int_{-\infty}^{\infty} \frac{dq}{2\pi} R_\nu(q|k) e^{iqx + i\alpha_0(q,\omega)z} . \tag{3.11}$$

The corresponding field in the region $z < \min h(x)$ is

$$\Phi_\nu^-(x, z|\omega) = \int_{-\infty}^{\infty} \frac{dq}{2\pi} T_\nu(q|k) e^{iqx - i\alpha(q,\omega)z} , \tag{3.12}$$

where

$$\alpha(q, \omega) = \sqrt{\epsilon(\omega)\frac{\omega^2}{c^2} - q^2} \quad , \quad \mathrm{Re}\,\alpha \,, \mathrm{Im}\,\alpha > 0 . \tag{3.13}$$

Here $R_\nu(q|k)$ and $T_\nu(q|k)$ denote the amplitudes of the reflected and transmitted waves, respectively.

If the incident field has a finite width, the above expressions change somewhat. The incident field can then be written as a weighted sum of plane waves where the weight distribution is contained in an envelope function $F(k)$. The incident field is

$$\Phi_\nu^{inc}(x,z|\omega) = \int_{-\frac{\omega}{c}}^{\frac{\omega}{c}} \frac{dk}{2\pi} F(k) e^{ikx - i\alpha_0(k,\omega)z} , \tag{3.14}$$

and the scattered field is

$$\Phi_\nu^{sc} = \int_{-\infty}^{\infty} \frac{dq}{2\pi} R_\nu(q,\omega) e^{iqx + i\alpha_0(q,\omega)z} , \tag{3.15}$$

where the reflection amplitude is

$$R_\nu(q,\omega) = \int_{-\frac{\omega}{c}}^{\frac{\omega}{c}} \frac{dk}{2\pi} R_\nu(q|k) F(k) . \tag{3.16}$$

The total far field above the surface, $z > \max\, h(x)$, is the sum of (3.14) and (3.15). Expressions for the transmitted field and the transmission amplitude are obtained in the same manner.

For this thesis, the so-called Gaussian finite beam is interesting since it represents a good approximation for a laser beam. These beams have a Gaussian envelope function. If the half-width of the incident beam is w, then the envelope can be expressed as [12]

$$F(k) = \frac{w\omega}{2\sqrt{\pi}c} \frac{1}{\alpha_0(k,\omega)} \exp\left[-\frac{w^2\omega^2}{4c^2} \left(\arcsin\frac{kc}{\omega} - \theta_0 \right)^2 \right] . \tag{3.17}$$

3.3 Mean differential reflection coefficient

The differential reflection coefficient is the fraction of the total incident power scattered into an angular interval $d\theta_s$ around the scattering angle θ_s. This is related to what is measured in the experiments. Using equation (2.14) and inserting the field in region $+$, equation (3.11), we get both the incident and scattered power. For a plane incident wave, they are respectively [10]

$$P^{inc} = \frac{L_x L_y}{2} \frac{c^2}{\omega} \alpha_0(k,\omega) , \tag{3.18}$$

and

$$P^{sc} = \frac{L_y}{2} \frac{c^2}{\omega} \int_{-\frac{\omega}{c}}^{\frac{\omega}{c}} \frac{dq}{2\pi} \alpha_0(q,\omega) |R_\nu(q|k)|^2 = \int_{-\frac{\pi}{2}}^{\frac{\pi}{2}} d\theta_s \, p^{sc}(\theta_s) , \tag{3.19}$$

where

$$p^{sc}(\theta_s) = \frac{L_y}{4\pi} \omega \cos^2\theta_s |R_\nu(q|k)|^2 . \tag{3.20}$$

Here, we have used that $q = \frac{\omega}{c}\sin\theta_s$. $p^{sc}(\theta_s)$ is the angular dependent scattered power. Thus we realize from the definition of the differential reflection coefficient that

$$\frac{\partial R_\nu}{\partial \theta_s} = \frac{p^{sc}(\theta_s)}{P^{inc}} = \frac{1}{L_x} \frac{\omega}{2\pi c} \frac{\cos^2\theta_s}{\cos\theta_0} |R_\nu(q|k)|^2 , \tag{3.21}$$

where we have used $k = \frac{\omega}{c}\sin\theta_0$ where θ_0 is the angle of incidence. However, if the surface is randomly rough, the mean differential reflection coefficient is the quantity of interest. We find the mean by averaging the differential reflection coefficient over an ensemble of surface realizations. Such a quantity is given by

$$\left\langle \frac{\partial R_\nu}{\partial \theta_s} \right\rangle = \left\langle \frac{p^{sc}(\theta_s)}{P^{inc}} \right\rangle = \frac{1}{L_x}\frac{\omega}{2\pi c}\frac{\cos^2\theta_s}{\cos\theta_0}\left\langle |R_\nu(q|k)|^2 \right\rangle \ , \tag{3.22}$$

where the brackets $\langle ... \rangle$ denote an ensemble average.

It is customary to separate $\langle \partial R_\nu/\partial\theta_s \rangle$ into two parts, one coherent and one incoherent term. This is done by rewriting

$$\left\langle |R_\nu(q|k)|^2 \right\rangle = |\langle R_\nu(q|k)\rangle|^2 + \left[\left\langle |R_\nu(q|k)|^2 \right\rangle - |\langle R_\nu(q|k)\rangle|^2 \right] \ , \tag{3.23}$$

where the first term on the right-hand side give rise to the coherent or specular contribution to $\langle \partial R_\nu/\partial\theta_s \rangle$, whereas the last term within the square brackets result in the incoherent or diffuse contribution.

For an incident beam with finite width, the expressions for power and the differential reflection coefficient change somewhat. The expressions for the incident and scattered power are [10]

$$P_{inc} = L_y \frac{wc}{2\sqrt{2\pi}} \left[\mathrm{erf}\left(\frac{w}{\sqrt{2}}\frac{\omega}{c}\left(\frac{\pi}{2} - \theta_0\right)\right) + \mathrm{erf}\left(\frac{w}{\sqrt{2}}\frac{\omega}{c}\left(\frac{\pi}{2} + \theta_0\right)\right)\right] \ , \tag{3.24}$$

where $\mathrm{erf}(x)$ is the error-function [15], and

$$p^{sc}(\theta_s) = L_y \frac{\omega}{2\pi^2}\cos^2\theta_s |R_\nu(q|k)|^2 \ , \tag{3.25}$$

respectively. Using the definition of the differential reflection coefficient (3.22), we get the following expression for the mean differential reflection coefficient for a incident beam of finite width

$$\left\langle \frac{\partial R_\nu}{\partial \theta_s} \right\rangle = \frac{2}{(2\pi)^{\frac{3}{2}}}\frac{\omega}{cw}\cos^2\theta_s \frac{\left\langle |R_\nu(q|k)|^2 \right\rangle}{\frac{1}{2}\left[\mathrm{erf}\left(\frac{w}{\sqrt{2}}\frac{\omega}{c}\left(\frac{\pi}{2} - \theta_0\right)\right) + \mathrm{erf}\left(\frac{w}{\sqrt{2}}\frac{\omega}{c}\left(\frac{\pi}{2} + \theta_0\right)\right)\right]} \ . \tag{3.26}$$

We can find corresponding expressions for the transmitted light in the same way as we did for the reflected light here. Such a procedure will result in the mean differential transmission coefficient $\left\langle \frac{\partial T_\nu}{\partial \theta_t} \right\rangle$. The only difference will be to change θ_s to θ_t and adjust for the dielectric function of the medium where the light is transmitted. Note that we in our case do not need to average since we are dealing with structured surface profiles.

The reflectance and the transmittance are obtained by integrating (3.22) and its equivalent for transmission over all angles

$$R_\nu = \int_{-\frac{\pi}{2}}^{\frac{\pi}{2}} d\theta_s \left\langle \frac{\partial R_\nu}{\partial \theta_s} \right\rangle \ , \tag{3.27}$$

and likewise to get the transmittance, T_ν. The sum of these two quantities is called *unitarity* and defined as

$$\mathcal{U} = \int_{-\frac{\pi}{2}}^{\frac{\pi}{2}} d\theta_s \left\langle \frac{\partial R_\nu}{\partial \theta_s} \right\rangle + \int_{-\frac{\pi}{2}}^{\frac{\pi}{2}} d\theta_t \left\langle \frac{\partial T_\nu}{\partial \theta_t} \right\rangle \ . \tag{3.28}$$

When no absorption takes place in either media, *i.e.* the imaginary part of the dielectric function is zero $\mathrm{Im}\{\epsilon\} = 0$, the unitarity should be one. This is a direct consequence of energy conservation. We have already seen this relation in equation (2.18).

3.4 Multilayer thin film scattering

The behavior of an electromagnetic wave propagating through layers of different media can be described by transfer matrices. For light at wavelength λ_0 and angle of incidence θ_0, the transfer matrix for a thin film with n layers is [13]

$$\begin{pmatrix} B \\ C \end{pmatrix} = \left\{ \prod_{m=1}^{n} \begin{bmatrix} \cos\delta_m & i\frac{\sin\delta_m}{\gamma_m} \\ i\gamma_m \sin\delta_m & \cos\delta_m \end{bmatrix} \right\} \begin{pmatrix} 1 \\ \gamma_{n+1} \end{pmatrix} . \tag{3.29}$$

Here, B and C represents the net electric and magnetic field at the first interface. The phase differences are defined as

$$\delta_m = \frac{2\pi}{\lambda_0} d_m n_m \cos\theta_m , \tag{3.30}$$

$$\gamma_m = \begin{cases} n_m \cos\theta_m , & s-\text{polarized} \\ \frac{n_m}{\cos\theta_m} , & p-\text{polarized} \end{cases} , \tag{3.31}$$

where d_m is the thickness of layer m, n_m is the complex refractive index of layer m and θ_m is obtained from Snell's law [8]. From (3.29) we find the reflection coefficient for a system with one layer between the initial and final media [13]

$$r = \frac{\gamma_0 \cos\delta + i\frac{\gamma_0\gamma_2}{\gamma_1}\sin\delta - i\gamma_1 \sin\delta - \gamma_2 \cos\delta}{\gamma_0 \cos\delta + i\frac{\gamma_0\gamma_2}{\gamma_1}\sin\delta + i\gamma_1 \sin\delta + \gamma_2 \cos\delta} . \tag{3.32}$$

By squaring the reflection coefficient, equation (3.32), we find the reflectance

$$R = r^* r , \tag{3.33}$$

where $*$ denotes the complex conjugate.

We will use the multilayer reflectance to compare one and two layer simulations.

Chapter 4

Numerical simulation approach

Only for ideal conditions the surface scattering problem can be solved exactly in an analytical fashion. To determine the total field $\Phi_\nu^\pm(x, z|\omega)$ for all points in space is a tremendous task, excluding the plane surface case. Various techniques like many-body perturbation theory and the reduced Rayleigh equation can be used [10]. However, if the surface is too rough, higher order scattering processes become important. As a consequence, the boundary conditions are dominated by non-local effects. That is, the total field at some point at the surface becomes dependent on the total field at other points at the surface. To overcome this problem, we have to resort to a rigorous numerical approach.

The method presented here is based on deriving coupled integral equations to determine the source functions, fields and its normal derivatives. With these quantities known, we can calculate the total field anywhere with the *Ewald-Oseen extinction theorem*. In the following chapter, we will outline how we do this numerically. This derivation follows closely that of Simonsen [10], from where also more details about the method can be found.

4.1 The Extinction Theorem

The Ewald-Oseen extinction theorem states that when an electromagnetic field enters a dispersive medium from vacuum, the incident field is extinguished by interference and replaced by another field propagating at a characteristic velocity for the dispersive medium [6]. We will here derive a mathematical expression for this by using *Green's functions*.

We start with the Helmholtz equation for the primary field (2.7) with an external source term added

$$\left(\nabla^2 + \epsilon(\omega)\frac{\omega^2}{c^2}\right)\Phi_\nu(\mathbf{r}|\omega) = -J_\nu^{ext}(\mathbf{r},\omega)\ , \tag{4.1}$$

where $-J_\nu^{ext}(\mathbf{r},\omega)$ is the external source term. The Green's function, $G(\mathbf{r}|\mathbf{r}';\omega)$, appropriate to (4.1) satisfies [6]

$$\left(\nabla^2 + \epsilon(\omega)\frac{\omega^2}{c^2}\right)G(\mathbf{r}|\mathbf{r}';\omega) = -4\pi\delta(\mathbf{r}-\mathbf{r}')\ . \tag{4.2}$$

Furthermore, we are only interested in out-going solutions to this equation that satisfy

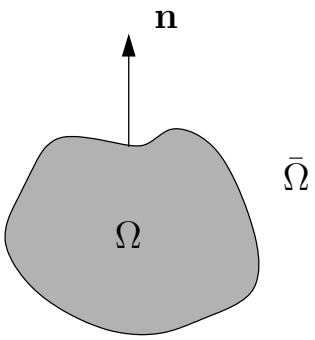

Figure 4.1: Illustration of the geometry used in derivation of the extinction theorem. Ω is an isotropic, homogeneous dielectric, while $\bar{\Omega}$ is the surrounding region containing the external source. $\mathbf{n}$ is a unit normal vector pointing from Ω into $\bar{\Omega}$.

Sommerfeld's radiation condition [14]

$$\lim_{r\to\infty} r(\partial_r G - ikG) = 0 \,, \tag{4.3}$$

where $r = |\mathbf{r}|$, $k = \omega/c$ is the wavenumber and ∂_r denotes a partial derivative with respect to r.

The two-dimensional solution to (4.2) that fulfills (4.3) is [6, 10]

$$G(\mathbf{r}|\mathbf{r}';\omega) = i\pi H_0^{(1)}\left(\sqrt{\epsilon(\omega)}\frac{\omega}{c}|\mathbf{r}-\mathbf{r}'|\right) \,, \tag{4.4}$$

where $H_0^{(1)}(\zeta)$ is the *Hankel-function* of first kind and zeroth order [15] and $\mathbf{r} = (x, z)$.

We consider a isotropic, homogeneous dielectric in region Ω surrounded by a region $\bar{\Omega}$, see figure 4.1. The boundary of the dielectric $\partial\Omega$ as well as the boundary at infinity is contained within the boundary of the surrounding region $\partial\bar{\Omega}$. We assume that the external source $J_\nu^{ext}(\mathbf{r},\omega)$ is located somewhere in $\bar{\Omega}$, while no sources are located within Ω.

Multiplying equation (4.1) by $G(\mathbf{r}|\mathbf{r}';\omega)$ and equation (4.2) by $-\Phi_\nu(\mathbf{r}|\omega)$, adding the resulting equations and then integrating over the exterior region $\bar{\Omega}$ yields

$$\begin{aligned} -\frac{1}{4\pi}\int_{\bar{\Omega}} d\mathbf{r}' \, \left[\Phi_\nu(\mathbf{r}'|\omega)\partial_{\mathbf{r}'}^2 G(\mathbf{r}'|\mathbf{r};\omega) - \partial_{\mathbf{r}'}^2\Phi_\nu(\mathbf{r}'|\omega)G(\mathbf{r}'|\mathbf{r};\omega)\right] \\ = -\frac{1}{4\pi}\int_{\bar{\Omega}} d\mathbf{r}' \, J_\nu^{ext}(\mathbf{r}',\omega)G(\mathbf{r}'|\mathbf{r};\omega) + \begin{cases} \Phi_\nu(\mathbf{r}|\omega) \,, & \mathbf{r}\in\bar{\Omega} \\ 0 \,, & \mathbf{r}\in\Omega \end{cases} \,, \end{aligned} \tag{4.5}$$

where we have interchanged $\mathbf{r}'$ and $\mathbf{r}$ for later convenience. The first term on the right-hand side of this equation is in fact the incident field due to the source, that is

$$-\frac{1}{4\pi}\int_{\bar{\Omega}} d\mathbf{r}' \, J_\nu^{ext}(\mathbf{r}',\omega)G(\mathbf{r}'|\mathbf{r};\omega) = \Phi_\nu^{inc}(\mathbf{r}|\omega) \,. \tag{4.6}$$

Furthermore, we use Green's second integral identity [6] to rewrite equation (4.5) as

$$\begin{aligned} \Phi_\nu^{inc}(\mathbf{r}|\omega) + \frac{1}{4\pi}\int_{\partial\Omega} dS' \, \left[\Phi_\nu(\mathbf{r}'|\omega)\partial_{n'} G(\mathbf{r}|\mathbf{r}';\omega) - \partial_{n'}\Phi_\nu(\mathbf{r}'|\omega)G(\mathbf{r}|\mathbf{r}';\omega)\right] \\ = \begin{cases} \Phi_\nu(\mathbf{r}|\omega) \,, & \mathbf{r}\in\bar{\Omega} \\ 0 \,, & \mathbf{r}\in\Omega \end{cases} \,, \end{aligned} \tag{4.7}$$

where dS' is a surface element and ∂_n denotes the outward normal derivative to the surface $\partial\Omega$. We have here used Sommerfeld's radiation condition (4.3) due to the vanishing integral over the surface at infinity, thus reducing the expression to an integral over $\partial\Omega$. Moreover, we have utilized $\partial_n = -\partial_{\bar{n}}$.

With the right-hand side set to zero, equation (4.7) is the extinction theorem. By looking at this equation, we see that the incident field is extinguished by the induced field represented by the second term on the left-hand side. In addition, this equation enables us to calculate the field $\Phi_\nu(\mathbf{r}|\omega)$ at any point outside Ω by just performing a surface integral over $\partial\Omega$. However, we need to determine the integrand to do so. Hence, the scattering problem reduces to finding the field and its normal derivative at the surface.

4.2 The scattered and transmitted fields

We will now focus on how to find the field for the scattering geometry shown in figure 3.1. Region + corresponds to region $\bar{\Omega}$ in figure 4.1, while region − corresponds to region Ω. The boundary $\partial\Omega$ is described by the surface profile function $h(x)$. From the extinction theorem, equation (4.7), we can now find the scattered and transmitted fields respectively

$$\Theta(z-h(x))\Phi_\nu^+(\mathbf{r}) = \Phi_\nu^{inc}(\mathbf{r}) + \frac{1}{4\pi}\int dx'\gamma(x')\left[\Phi_\nu^+(\mathbf{r}')\partial_{n'}G_+(\mathbf{r}'|\mathbf{r}) - \partial_{n'}\Phi_\nu^+(\mathbf{r}')G_+(\mathbf{r}'|\mathbf{r})\right]\big|_{z=h(x)} \ , \quad (4.8a)$$

$$\Theta(h(x)-z)\Phi_\nu^-(\mathbf{r}) = -\frac{1}{4\pi}\int dx'\gamma(x')\left[\Phi_\nu^-(\mathbf{r}')\partial_{n'}G_-(\mathbf{r}'|\mathbf{r}) - \partial_{n'}\Phi_\nu^-(\mathbf{r}')G_-(\mathbf{r}'|\mathbf{r})\right]\big|_{z=h(x)} \ , \quad (4.8b)$$

where we have suppressed the explicit frequency dependence to ensure readability, and we will continue to suppress it. $\Theta(\zeta - a)$ denotes Heaviside's step function, and the superscripts $\pm$ indicate in which media the quantities are evaluated. Furthermore, we have defined the normal derivative in equation (3.6) where

$$\gamma(x) = \sqrt{1 + (h'(x))^2} \ . \quad (4.9)$$

The surface $h(x)$ is still assumed to be a single-valued function of x so that its surface element dS becomes

$$dS = \gamma(x)dx \ . \quad (4.10)$$

By taking the boundary conditions to be satisfied at the surface (3.4) and (3.7) into account, we see that the integral equations for the fields (4.8) become coupled. Hence, we get

$$\Theta(z-h(x))\Phi_\nu^+(\mathbf{r}) = \Phi_\nu^{inc}(\mathbf{r}) + \frac{1}{4\pi}\int dx'\left[A_+(\mathbf{r}|x')\mathcal{F}_\nu(x') - B_+(\mathbf{r}|x')\mathcal{N}(x)\right] \ , \quad (4.11a)$$

$$\Theta(h(x)-z)\Phi_\nu^-(\mathbf{r}) = -\frac{1}{4\pi}\int dx'\left[A_-(\mathbf{r}|x')\mathcal{F}_\nu(x') - \frac{\kappa_\nu^-}{\kappa_\nu^+}B_-(\mathbf{r}|x')\mathcal{N}(x)\right] \ , \quad (4.11b)$$

where $\kappa_\nu^\pm$ are defined in (3.8). $\mathcal{F}_\nu(x)$ and $\mathcal{N}_\nu(x)$ are defined as the source functions

$$\mathcal{F}_\nu(x) = \Phi_\nu^+(x,z)\,\big|_{z=h(x)} \ , \tag{4.12a}$$

$$\mathcal{N}_\nu(x) = \gamma(x)\partial_n \Phi_\nu^+(x,z)\,\big|_{z=h(x)} \ , \tag{4.12b}$$

while $A_\pm(\mathbf{r}|x')$ and $B_\pm(\mathbf{r}|x')$ are defined as kernels

$$A_\pm(\mathbf{r}|x') = \frac{1}{4\pi}\gamma(x')\partial_{n'} G_\pm(x,z|x',z')\,\big|_{z'=h(x')} \ , \tag{4.13a}$$

$$B_\pm(\mathbf{r}|x') = \frac{1}{4\pi} G_\pm(x,z|x',z')\,\big|_{z'=h(x')} \ . \tag{4.13b}$$

Inserting the Fourier representation for the Green's function [15]

$$G_+(\mathbf{r}|\mathbf{r}') = \int_{-\infty}^{\infty} \frac{dq}{2\pi}\,\frac{2\pi i}{\alpha_0(q)} e^{iq(x-x')+i\alpha_0(q)|z-z'|} \ , \tag{4.14}$$

into equations (4.13) and then into equation (4.11a), we find that the scattered field far above the surface, $z \gg h(x)$, can be written as

$$\Phi_\nu^{sc}(\mathbf{r}) = \int_{-\infty}^{\infty} \frac{dq}{2\pi}\, R_\nu(q) e^{iqx+i\alpha_0(q)z} \ , \tag{4.15}$$

where the scattering amplitude is given by

$$R_\nu(q) = \frac{i}{2\alpha_0(q)} \int_{-\infty}^{\infty} dx\, e^{-iqx-i\alpha_0(q)h(x)} \left[i\left\{ qh'(x) - \alpha_0(q) \right\} \mathcal{F}_\nu(x) - \mathcal{N}_\nu(x) \right] \ . \tag{4.16}$$

If the medium below the surface, $z \ll h(x)$, is transparent, we can find the transmitted field by using the Green's function, equivalent to (4.14), in a similar fashion as we found the scattered field. The transmitted field is thus

$$\Phi_\nu^{tr}(\mathbf{r}) = \int_{-\infty}^{\infty} \frac{dq}{2\pi}\, T_\nu(q) e^{iqx-i\alpha(q)z} \ , \tag{4.17}$$

where the transmission amplitude is given by

$$T_\nu(q) = -\frac{i}{2\alpha(q)} \int_{-\infty}^{\infty} dx\, e^{-iqx+i\alpha(q)h(x)} \left[i\left\{ qh'(x) + \alpha(q) \right\} \mathcal{F}_\nu(x) - \frac{\kappa_\nu^-}{\kappa_\nu^+} \mathcal{N}_\nu(x) \right] \ . \tag{4.18}$$

4.3 Determining the source functions

We have now changed the task of finding the field and its normal derivative to finding the source terms (4.12). This is done by introducing a small perturbation β to $h(x)$ in equations (4.8) and then letting $\beta \to 0^+$. In doing so, we obtain a coupled set of inhomogeneous integral equations for the sources

$$\mathcal{F}_\nu(x) = \mathcal{F}_\nu^{inc}(x) + \int dx' \ \left[\mathcal{A}_+(x|x')\mathcal{F}_\nu(x') - \mathcal{B}_+(x|x')\mathcal{N}_\nu(x') \right] \ , \tag{4.19a}$$

$$0 = \int dx' \ \left[\mathcal{A}_-(x|x')\mathcal{F}_\nu(x') - \frac{\kappa_\nu^-}{\kappa_\nu^+} \mathcal{B}_-(x|x')\mathcal{N}_\nu(x') \right] \ , \tag{4.19b}$$

where we have defined the new kernels as

$$\mathcal{A}_{\pm}(x|x') = \lim_{\beta\to 0^+} A_{\pm}(\mathbf{r}|x')\,\big|_{z=h(x)+\beta} \ , \tag{4.20a}$$

$$\mathcal{B}_{\pm}(x|x') = \lim_{\beta\to 0^+} B_{\pm}(\mathbf{r}|x')\,\big|_{z=h(x)+\beta} \ . \tag{4.20b}$$

$\mathcal{F}_{\nu}^{inc}(x)$ is defined from equation (4.12a) where we have replaced $\Phi_{\nu}^{+}(x,z)$ with the incoming field $\Phi_{\nu}^{inc}(x,z)$.

In order to solve equations (4.19), we convert the equations into matrix equations by discretizing the spatial variable x' to a grid with N cells. The length of the infinitely long surface is restricted to a finite length $\mathcal{L}$, thus making the cell size $\Delta\xi = \mathcal{L}/N$. Finally, we define the spatial integration to range from $-\mathcal{L}/2$ to $\mathcal{L}/2$. With these definitions, we can express the grid as

$$\xi_n = -\frac{\mathcal{L}}{2} + \left(n - \frac{1}{2}\right)\Delta\xi \ , \quad n = 1, 2, 3, ..., N \ . \tag{4.21}$$

By assuming that the source functions vary slowly over one cell, we can consider them as constant over this spatial interval. This way, we can put them outside the integral and rewrite equations (4.19) to the following matrix equations by setting $x = \xi_m$

$$\mathcal{F}_{\nu}(\xi_m) = \mathcal{F}_{\nu}^{inc}(\xi_m) + \sum_{n=1}^{N}\left[\mathcal{A}_{mn}^{+}\mathcal{F}_{\nu}(\xi_n') - \mathcal{B}_{mn}^{+}\mathcal{N}_{\nu}(\xi_n')\right] \ , \tag{4.22a}$$

$$0 = \sum_{n=1}^{N}\left[\mathcal{A}_{mn}^{-}\mathcal{F}_{\nu}(\xi_n') - \frac{\kappa_{\nu}^{-}}{\kappa_{\nu}^{+}}\mathcal{B}_{mn}^{-}\mathcal{N}_{\nu}(\xi_m')\right] \ , \tag{4.22b}$$

where the matrix elements $\mathcal{A}_{mn}^{\pm}$ and $\mathcal{B}_{mn}^{\pm}$ are defined as

$$\mathcal{A}_{mn}^{\pm} = \int_{\xi_n-\Delta\xi/2}^{\xi_n+\Delta\xi/2} dx'\ \mathcal{A}_{\pm}(\xi_m|x') \ , \tag{4.23a}$$

$$\mathcal{B}_{mn}^{\pm} = \int_{\xi_n-\Delta\xi/2}^{\xi_n+\Delta\xi/2} dx'\ \mathcal{A}_{\pm}(\xi_m|x') \ . \tag{4.23b}$$

The kernels (4.20) contains the Hankel function $H_0^{(1)}(\zeta)$ and its normal derivative which are singular when their arguments vanish, $\zeta = 0$. Therefore, we have to be careful when treating the kernels as they are also singular at $x = x'$. Fortunately, these singularities are integrable so that the matrix elements (4.23) are well defined everywhere. From [10] we get the following expressions for the matrix elements (4.23)

$$\mathcal{A}_{mn}^{\pm} = \begin{cases} \Delta\xi A_{\pm}(\xi_m|\xi_n) \ , & m \neq n \ , \\ \frac{1}{2} + \Delta\xi\frac{h''(\xi_m)}{4\pi\gamma^2(\xi_m)} \ , & m = n \ , \end{cases} \tag{4.24a}$$

and

$$\mathcal{B}_{mn}^{\pm} = \begin{cases} \Delta\xi B_{\pm}(\xi_m|\xi_n) \ , & m \neq n \ , \\ -\frac{i}{4}\Delta\xi H_0^{(1)}\left(\sqrt{\epsilon_{\pm}}\frac{\omega}{c}\frac{\gamma(\xi_m)\Delta\xi}{2e}\right) \ , & m = n \ , \end{cases} \tag{4.24b}$$

where $\gamma(x)$ is defined in equation (4.9).

The matrix equations for the source functions (4.22), together with the matrix elements (4.24), can be solved numerically by standard techniques from linear algebra [16].

From this, we obtain the source functions which in turn enable us to find the scattering amplitude (4.16) and, if applicable, the transmission amplitude (4.18). With the amplitudes known, we can determine the physically observable quantities, like the (mean) differential reflection coefficient (3.22). Hence, we have solved the scattering problem.

Chapter 5

Hydrodynamics

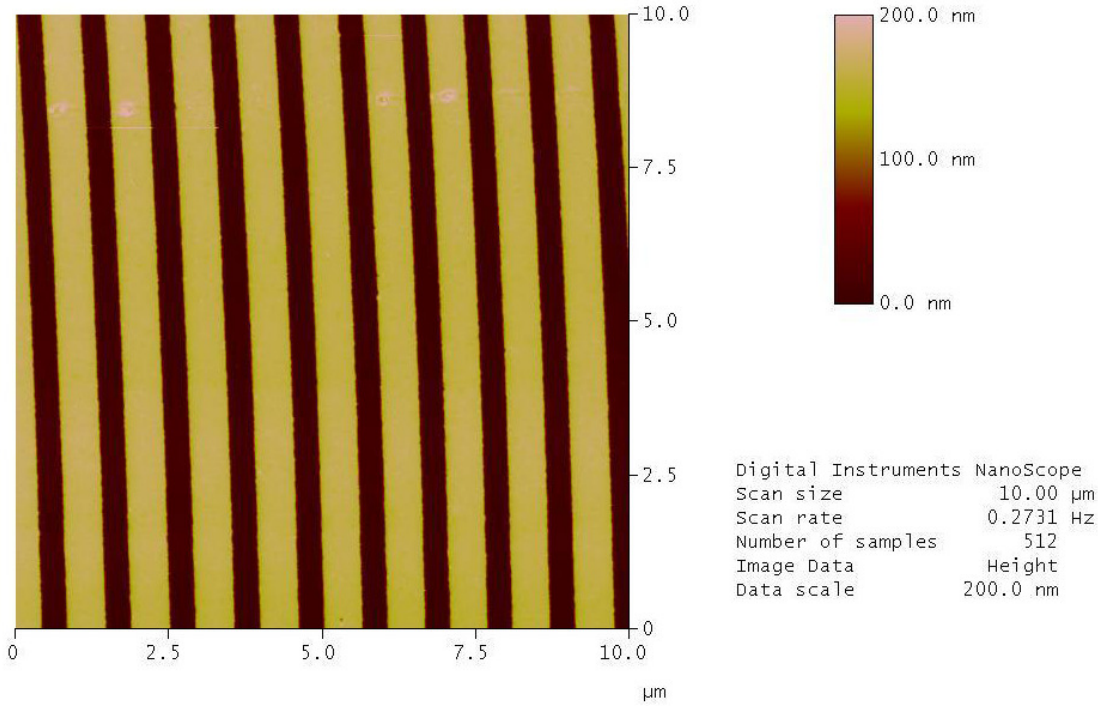

Figure 5.1: AFM image of an imprinted surface, seen from above. The periodicity in the x-direction is clearly seen. The figure is taken from Reference [2].

The surfaces of our experimental samples are periodic in the x-direction and constant in the y-direction (see figure 5.1), making our problem effectively one-dimensional. When heated above the glass transition temperature, a *relaxation process* will gradually smoothen the surface, and in time make it completely flat. This change in surface structure is governed by hydrodynamics, and the important material parameters controlling this process are surface tension and viscosity.

In this section we plan to describe the relaxation process. We introduce the *stream function* and find its general form for the system treated in this thesis. The general boundary conditions are derived and we briefly explain the concepts of perturbation theory and the glass transition temperature.

5.1 Fundamental equations

Conservation of mass is a fundamental part of hydrodynamics. It is elegantly described by the *continuity equation* [17]

$$\frac{\partial \rho_m}{\partial t} + \nabla \cdot (\rho_m \mathbf{v}) = 0 \,, \tag{5.1}$$

where ρ_m is the mass density of the fluid and $\mathbf{v} = (u, v, w)$ is the velocity field of the fluid. Notice the similarity to the continuity equation for electromagnetic charge and current (2.4). For *incompressible flow*, the mass density can be treated as constant, and thus the continuity equation (5.1) reduces to

$$\nabla \cdot \mathbf{v} = 0 \,. \tag{5.2}$$

The equations of motion of an incompressible viscous fluid are called *Navier-Stokes equations* [18]

$$\rho_m \frac{\mathrm{d}\mathbf{v}}{\mathrm{d}t} = \eta \nabla^2 \mathbf{v} - \nabla p - \nabla \phi \,, \tag{5.3}$$

where $\frac{\mathrm{d}}{\mathrm{d}t} = \frac{\partial}{\partial t} + \mathbf{v} \cdot \nabla$, p is the pressure field and η is the viscosity of the fluid. The $\nabla\phi$ term is added to include forces acting on the fluid, if applicable. Examples of such forces include gravity, van der Waals forces etc.

Viscous behavior for fluids is described by the *Reynolds number*

$$\mathrm{Re} = \frac{vl}{\nu} \,, \tag{5.4}$$

where v and l are the characteristic velocity and length of the system, and $\nu = \eta/\rho_m$ is the kinematic viscosity. For very small Reynolds numbers, $0 < \mathrm{Re} < 1$, we have so-called *creeping flow* where effects of inertia can be neglected. Medium range values, $1 < \mathrm{Re} < 10^3$ yield smooth laminar flow, whereas very high Re, *i.e.* $10^4 < \mathrm{Re}$, usually means turbulent flow [19]. In the range $10^3 < \mathrm{Re} < 10^4$ we have transition from laminar to turbulent flow.

The ratio of $\rho_m \frac{\mathrm{d}\mathbf{v}}{\mathrm{d}t}$ and $\eta \nabla^2 \mathbf{v}$ is vl/ν, which is exactly the Reynolds number. Here we treat creeping flow, hence equation (5.3), reduces to the simpler form

$$\nabla p = \eta \nabla^2 \mathbf{v} \,. \tag{5.5}$$

This is the equation of motion for creeping flow, where the $\nabla\phi$ term is omitted for simplicity.

The *stress tensor* of a fluid can be written as [17]

$$\sigma_{ik} = -p\delta_{ik} + \sigma'_{ik} \,, \tag{5.6}$$

where σ'_{ik} is the viscous stress tensor and δ_{ik} denotes the Kronecker δ-function defined so that it is 1 if $i = k$ and 0 otherwise. σ'_{ik} is a symmetric tensor, meaning $\sigma'_{ik} = \sigma'_{ki}$, and for an incompressible fluid it can be written in terms of velocity gradients [17]

$$\sigma'_{ik} = \eta \left(\frac{\partial v_i}{\partial x_k} + \frac{\partial v_k}{\partial x_i} \right) \,. \tag{5.7}$$

The stress tensor σ_{ik} represents the force in direction i on a surface oriented in direction k.

Navier-Stokes equations are nonlinear partial differential equations with four unknown variables, p and the three components of $\mathbf{v}$. Combining them with the incompressible continuity equation (5.2) yields four equations with four unknown variables. It is non-trivial to solve this system analytically, though it is possible through assumptions and approximations.

5.2 The stream function

For two-dimensional incompressible flow, it is possible to reduce Navier-Stokes equations (5.3) and the continuity equation (5.1) to equations of two variables (p,ψ) instead of four (p,$\mathbf{v}$) by introducing the stream function $\psi = \psi(x, z)$. The incompressibility condition (5.2) in two dimensions is satisfied if the stream function is defined as [19]

$$u = \frac{\partial \psi}{\partial z} , \quad w = -\frac{\partial \psi}{\partial x} . \tag{5.8}$$

It can be shown by using vector identities that [19]

$$\nabla \times \mathbf{v} = -\hat{\mathbf{y}} \nabla^2 \psi , \tag{5.9}$$

where $\hat{\mathbf{y}}$ is the unit vector in the y-direction.

The stream function gives the stream lines of the flow. These are tangential to the velocity field at any time, and the difference of two stream lines equals the volume flow between these two lines.

Taking the curl on both sides of equation (5.5) yields

$$\nabla^4 \psi = 0 , \tag{5.10}$$

due to the vanishing curl of a divergence and equation (5.9). A general solution to this biharmonic equation is obtained by assuming that the stream function is separable in x and z. The resulting stream function becomes

$$\psi(x, z) = \Big[(b_+ z + c_+) \exp(kz) + (b_- z + c_-) \exp(-kz) \Big] \cos(kx) , \tag{5.11}$$

where $b_\pm$ and $c_\pm$ are constants to be determined by boundary conditions. In equation (5.11) we have imposed the periodicity in the x-direction through the cosine factor. $k = 2\pi/L$ where L is the period of the surface.

5.3 Boundary conditions at a two-fluid interface

At the interface between two fluids in equilibrium, the forces of viscous friction must be equal on both sides. If the surface is curved, surface tension also has to be taken into account. This can be expressed as

$$\left(\sigma_{ik}^{(-)} - \sigma_{ik}^{(+)} \right) n_k = \gamma \kappa n_i , \tag{5.12}$$

where γ is the surface tension coefficient (not related to the function $\gamma(x)$ defined in equation (4.9)), κ is the curvature of the surface, n_i and n_k are normal unit vector components to the surface and the indices + and – refer to the fluids on the two sides of the interface, see figure 2.2. Writing out the normal and tangential components of

equation (5.13) yields the following general boundary conditions for an interface with constant surface tension

$$n_i\sigma_{ik}^{(-)}n_k - n_i\sigma_{ik}^{(+)}n_k = \gamma\kappa \,, \tag{5.13a}$$

$$t_i\sigma_{ik}^{(-)}n_k - t_i\sigma_{ik}^{(+)}n_k = 0 \,. \tag{5.13b}$$

Here t_i is the tangential unit vector component to the surface. The normal and tangential unit vectors are defined as [11]

$$\mathbf{n} = \frac{(-h'(x), 0, 1)}{\sqrt{1 + (h'(x))^2}} \,, \tag{5.14}$$

$$\mathbf{t} = \frac{(1, 0, h'(x))}{\sqrt{1 + (h'(x))^2}} \,, \tag{5.15}$$

$$\kappa = \frac{h''(x)}{\left(1 + (h'(x))^2\right)^{3/2}} \,, \tag{5.16}$$

where $z = h(x)$ defines the interface.

A *free surface* is an interface between two fluids where the tangential stress for at least one of the fluids is essentially zero [20]. This is the situation here, where one of the fluids is air with practically no viscosity. Thus, the stress tensor for air reduces to

$$\sigma_{ik}^{(+)} = -p_0\delta_{ik} \,, \tag{5.17}$$

where p_0 is the atmospheric pressure. This simplifies the general boundary conditions (5.13) for the considered system to

$$n_i\sigma_{ik}^{(-)}n_k + p_0 = \gamma\kappa \,, \tag{5.18a}$$

$$t_i\sigma_{ik}^{(-)}n_k = 0 \,. \tag{5.18b}$$

Hence, the boundary conditions at a free surface expressed in terms of the stream function (5.11) become

$$\frac{2\eta}{\sqrt{1 + (\partial_x h)^2}}\Big(\left[1 - (\partial_x h)^2\right]\partial_x\partial_z\psi - (\partial_x h)\left[\partial_x^2\psi - \partial_z^2\psi\right]\Big) + p - p_0 = -\gamma\kappa \,, \tag{5.19a}$$

$$\frac{4\eta}{\sqrt{1 + (\partial_x h)^2}}(\partial_x h)\partial_x\partial_z\psi + \frac{\eta}{\sqrt{1 + (\partial_x h)^2}}\left[1 - (\partial_x h)^2\right]\left(\partial_x^2\psi - \partial_z^2\psi\right) = 0 \,. \tag{5.19b}$$

Both boundary conditions are evaluated at the surface $z = h(x)$.

5.4 Perturbation theory

For samples where the surface profile $h(x)$ satisfies

$$k|h(x,t)| \ll 1 \,, \tag{5.20a}$$

$$|\partial_x h(x,t)| \ll 1 \,, \tag{5.20b}$$

perturbation theory can be used to study the surface evolution. This method is inspired by Reference [21], where wave scattering from randomly rough surfaces is treated at the

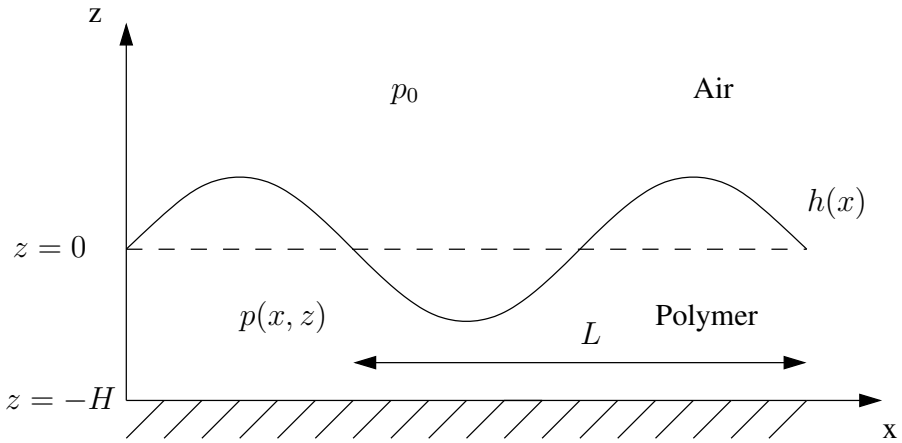

Figure 5.2: Illustration of the system treated in the stream function model. $h(x)$ is the polymer surface with mean height $z = 0$ (dashed line). $p(x, z)$ and p_0 are the pressure distributions of the polymer and air respectively. $z = -H$ denotes the polymer/substrate boundary and L is the period.

mean value of the surface. The restrictions expressed by equations (5.20) say that the surface does not deviate too much from the mean height. We assume that quantities that are functions of the surface profile can be expanded as Taylor series around some mean value of the surface. The mean value of a surface $h(x)$ is defined as

$$\langle h \rangle = \frac{1}{L} \int_{-L/2}^{L/2} \mathrm{d}x \, h(x) \, , \tag{5.21}$$

where L is the period of the surface.

For mean height $z = 0$ in Figure 5.2 the Taylor expansion of these quantities reads

$$f(x, h) = f(x, 0) + h\partial_z f(x, 0) + \frac{h^2}{2!}\partial_z^2 f(x, 0) + ... \tag{5.22}$$

In our case, the quantities $f(x, h)$ may be the stream function, the pressure, the stress tensor and so on.

One of the advantages of using perturbation theory is that it makes analytical solutions easy to obtain. Although these solutions are approximative solutions, they can give valuable qualitative information.

5.5 Glass transition temperature

The glass transition temperature, T_g, is the temperature where an amorphous solid, like a polymer, becomes soft on heating. Below this temperature, the bonds between the polymer chains are intact. Above T_g the bonds start to break, making the polymer bendable and thus ductile. Figure 1.4 shows the transition by the sudden decrease of viscosity for different molecular weights of the polymer. The transition around 120°C is clearly visible only for the two heaviest polymers.

Chapter 6

Relaxation process

Since the surface profiles we are concerned with in this work are periodic with period L, they can be described by a Fourier series [22]

$$h(x,t) = \sum_{n=0}^{\infty} \left[a_n(t) \cos\left(\frac{2\pi n x}{L}\right) + b_n(t) \sin\left(\frac{2\pi n x}{L}\right) \right] . \tag{6.1}$$

Including all terms with suitable choices of coefficients $a_n(t)$ and $b_n(t)$ will give a square wave profile like those produced by nanolithography imprinting. Experimentally, it has been demonstrated that the higher order modes (large n) relax and disappear rather quickly. Hence, the evolution of the surface profile in equation (6.1) can be determined by treating the lower order modes (small n).

The temperature distribution over the polymer film is considered uniform and time independent. Hence, energy transport caused by temperature gradients can be neglected.

Figure 5.2 illustrates our sample. A polymer with a free surface at $z = h(x,t)$ is heated to a temperature above the glass transition temperature T_g. In the region $-H \leq z \leq h(x,t)$ the polymer film is present. A solid substrate with good adhesive properties is placed below the polymer film, $z \leq -H$. The region above the polymer film, $z \geq h(x,t)$, is air. Here, we include the time-dependence from now on because the surface is relaxing as time evolves.

6.1 Stream function model

The stream function model assumes incompressible creeping flow. Thus, the equation of motion (5.5) is in component form and in terms of the stream function

$$\frac{\partial p}{\partial x} = \eta \frac{\partial}{\partial z} \left(\frac{\partial^2 \psi}{\partial x^2} + \frac{\partial^2 \psi}{\partial z^2} \right) , \tag{6.2a}$$

$$\frac{\partial p}{\partial z} = -\eta \frac{\partial}{\partial x} \left(\frac{\partial^2 \psi}{\partial x^2} + \frac{\partial^2 \psi}{\partial z^2} \right) . \tag{6.2b}$$

We neglect gravity due to the small thickness of the film. The hydrostatic pressure p in a fluid in a gravitational field is [17]

$$p = p_0 - \rho_m g z , \tag{6.3}$$

where p_0 is the atmospheric pressure. Surface tension is omitted for simplicity. For small polymer film thickness, H, as is assumed in our study, the pressure difference between the surface $z = h(x,t)$ and the polymer/substrate boundary is very small compared to p_0. Thus, we may neglect the gravitational contribution relative to the atmospheric pressure. Hence, equations (6.2) are valid.

We are only considering the lowest order term of the perturbation theory, *e.g.* we evaluate the boundary conditions at the mean value of the surface, $z = 0$, and we assume $\partial_x h \ll 1$ and $kh \ll 1$. This makes our model linear in the surface profile $h(x,t)$. A practical choice of surface profile is the fundamental mode of the sine-part of equation (6.1)

$$h(x,t) = \tilde{h}(t)\sin(kx)\ , \tag{6.4}$$

where $\tilde{h}(t)$ is the time-dependent amplitude of the surface profile.

6.1.1 Boundary conditions

The stream function, ψ, is essential to this model. It is defined by the partial differential equation (5.10), and the solution in our case is defined in equation (5.11) which contains four unknown coefficients to be determined, $b_\pm$ and $c_\pm$. This requires four boundary conditions. We get two from the normal and tangential stresses, equations (5.19a) and (5.19b) respectively, and two more from assuming no slip and no penetration at the polymer/substrate boundary ($\mathbf{v}(x,z)|_{z=-H} = 0$). Considering only the lowest order term of the perturbation theory ($\partial_x h \ll 1$ and $kh \ll 1$) simplifies the boundary conditions and enables us to evaluate them at the mean height of the surface $z = 0$. The boundary conditions within these approximations are

$$\partial_z \psi(x,z)|_{z=-H} = 0\ , \tag{6.5a}$$

$$\partial_x \psi(x,z)|_{z=-H} = 0\ , \tag{6.5b}$$

$$\eta\left(\partial_z^2\psi - \partial_x^2\psi\right)\big|_{z=0} = 0 \tag{6.5c}$$

and

$$p(x,z)|_{z=0} - p_0 = -\gamma\partial_x^2 h\ . \tag{6.5d}$$

In the *small slope approximation* $\partial_x h \ll 1$, there should also be a viscous term $(2\eta\ \partial_x\partial_z\psi|_{z=0})$ at the left hand side of boundary condition (6.5d). However, this term is omitted due to the creeping flow character of the fluid ($\partial_x\psi = -w \ll 1$). That is, the pressure dominates normal stress and we are left with boundary condition (6.5d).

6.1.2 Determination of the coefficients $b_\pm$ and $c_\pm$

By integrating equation (6.2a) with respect to x and equation (6.2b) with respect to z and inserting the stream function (5.11), we get the pressure distribution within the polymer

$$p(x,z) - p_0 = 2\eta k\left[b_+\exp(kz) + b_-\exp(-kz)\right]\sin kx\ . \tag{6.6}$$

The lack of the coefficients $c_\pm$ in this expression does not mean they are zero. They are still present via the boundary conditions (6.5a), (6.5b) and (6.5c).

Now we have all expressions needed to determine the unknown coefficients, $b_\pm$ and $c_\pm$. Calculating all needed derivatives of the stream function and evaluating them at

the proper z-values according to the boundary conditions (6.5) yields three equations. The fourth equation comes from inserting the pressure distribution (6.6) and the surface profile (6.4) into the fourth boundary condition (6.5d). We are left with a linear set of four equations for the four unknown coefficients

$$\begin{bmatrix} -HE_- & -HE_+ & E_- & E_+ \\ (1-kH)E_- & (1+kH)E_+ & kE_- & -kE_+ \\ 1 & 1 & 0 & 0 \\ -1 & 1 & -k & -k \end{bmatrix} \begin{bmatrix} b_+ \\ b_- \\ c_+ \\ c_- \end{bmatrix} = \begin{bmatrix} 0 \\ 0 \\ \frac{\gamma k\tilde{h}}{2\eta} \\ 0 \end{bmatrix} , \tag{6.7}$$

where $E_\pm = \exp(\pm kH)$.

Solving this system of equations yields

$$b_\pm = \frac{\gamma k\tilde{h}}{2\eta}\left(\frac{\exp(\pm 2kH) \mp 4kH + 2}{[\exp(kH)+\exp(-kH)]^2}\right) , \tag{6.8a}$$

$$c_\pm = \frac{\gamma\tilde{h}}{2\eta}\left(\frac{\mp(\exp(\pm 2kH)+1) \mp 2k^2H^2 + 2kH}{[\exp(kH)+\exp(-kH)]^2}\right) . \tag{6.8b}$$

Note that $b_\pm$ and $c_\pm$ are time-dependent due to $\tilde{h} = \tilde{h}(t)$ and that they are inversely proportional to the viscosity, $b_\pm$ and $c_\pm \sim 1/\eta$.

6.1.3 Evolution of surface profile

The vertical velocity of the surface in the form of equation (6.4) is

$$w = \frac{\mathrm{d}h}{\mathrm{d}t} = \frac{\partial h}{\partial t} + u\frac{\partial h}{\partial x} . \tag{6.9}$$

When inserting the stream function relation to velocity (5.8) and applying the assumption $\partial_x h \ll 1$, this reduces to

$$-\frac{\partial \psi}{\partial x} = \frac{\partial h}{\partial t} . \tag{6.10}$$

By using the stream function (5.11) and the surface profile (6.4) together with equation (6.10) and then evaluating the resulting expression at the mean height $z = 0$, we get

$$\frac{\partial \tilde{h}}{\partial t} = k(c_+ + c_-) . \tag{6.11}$$

Substituting the coefficients (6.8b) and solving this differential equation, the time dependent amplitude of the surface profile is obtained

$$\tilde{h}(t) = \tilde{h}_0 \exp(-t/\tau) . \tag{6.12}$$

Here, $\tilde{h}_0 = \tilde{h}(t=0)$ is the initial surface amplitude and τ is the characteristic relaxation time of the surface profile given by

$$\tau = \frac{2\eta}{\gamma k}\frac{\exp(2kH)+\exp(-2kH)+2}{\exp(2kH)-\exp(-2kH)-4kH} . \tag{6.13}$$

Observe that the relaxation time is linearly proportional to the viscosity, $\tau \sim \eta$. As it turns out, this linear dependence will simplify the task of finding the temperature dependent viscosity, $\eta(T)$. Finally, we use the expression for the surface amplitude (6.12) with the surface profile (6.4), and end up with the evolution equation of the surface

$$h(x,t) = \tilde{h}_0 \exp(-t/\tau)\sin(kx) . \tag{6.14}$$

6.2 Dimensional analysis

Here, we discuss the possible combinations of the appropriate physical parameters that give dimension time. This will tell us if there are other connections between relaxation time and viscosity, besides the linear connection. The only appropriate physical parameters[2] here are the surface tension γ, the viscosity η and the period of the system l. A combination of these parameters will give the relaxation time, *i.e.*

$$\tau \sim \eta^{\alpha}\gamma^{\beta}l^{\sigma} \,, \tag{6.15}$$

where α, β and σ are real numbers to be determined. By looking at the dimensions of each physical parameter, we get enough equations to determine these numbers. These are

$$[\tau] = \mathrm{s} \,, \tag{6.16a}$$
$$[\eta] = \frac{\mathrm{kg}}{\mathrm{ms}} \,, \tag{6.16b}$$
$$[\gamma] = \frac{\mathrm{kg}}{\mathrm{s}^2} \,, \tag{6.16c}$$
$$[l] = \mathrm{m} \,. \tag{6.16d}$$

Applying these with equation (6.15) yields the following equation for the dimension

$$\begin{aligned}[\tau] &= [\eta]^{\alpha}[\gamma]^{\beta}[l]^{\sigma} \\ &= \left(\frac{\mathrm{kg}}{\mathrm{ms}}\right)^{\alpha}\left(\frac{\mathrm{kg}}{\mathrm{s}^2}\right)^{\beta} m^{\sigma} \\ &= \mathrm{kg}^{\alpha+\beta}s^{-\alpha-2\beta}m^{\sigma-\alpha} \,,\end{aligned} \tag{6.17}$$

which in turn yields three equations for the numbers due to (6.16a)

$$\alpha + \beta = 0 \,, \tag{6.18a}$$
$$\alpha + 2\beta = -1 \,, \tag{6.18b}$$
$$\sigma - \alpha = 0 \,. \tag{6.18c}$$

This set of equation solves to $\alpha = 1$, $\beta = -1$ and $\sigma = 1$. Inserting these numbers into equation (6.15) yields

$$\tau \sim \frac{\eta}{\gamma k} \,, \tag{6.19}$$

where $k \sim 1/l$ is used to easier relate this result to the already obtained expression for the relaxation time (6.13). We see that these two results are essentially the same. Equation (6.19) is the only possible solution under these conditions. Hence, the relaxation is linearly dependent on viscosity. However, this method cannot exclude viscosity factors appearing in exponential factors, *e.g.* if the relaxation time is on the form $\tau \sim \eta \exp(\eta/A)$, where A is a constant of appropriate dimension.

[2]Strictly speaking from a dimensional analysis point of view, we should also include the thickness of the polymer film, H. However, excluding this parameter from the dimensional analysis will not change anything physically because the mean value of H is constant in our experiments.

Chapter 7

Method

In this section we will describe how we simulate scattering from a relaxing surface, how the experimental data is obtained and how we combine these to determine the temperature dependent viscosity, $\eta(T)$.

7.1 Electromagnetic scattering simulation

Our scattering simulation method is quite powerful as we can include as many layers of different materials as we wish, look at different angles of incidence and different wavelengths. There is virtually no restriction besides the computer's memory to what we can include. Larger systems, higher temporal resolution and higher spatial discretization will understandably require more computation time.

The initial profiles used in the experiments have steep profiles as shown in figure 1.1(c). To recreate this for the simulations, we use a Gaussian-like function

$$h(x,t) = h(t) \sum_{n=-\infty}^{\infty} \exp\left[-\left(\frac{x - \left(n - \frac{1}{2}\right) L}{\Delta x} \right)^6 \right], \tag{7.1}$$

where $h(t)$ is the time-dependent amplitude, L is the period and Δx is the width of the profile's peak. Combining several of these functions in a row resemble the experimental profiles without being too steep. If the simulation profile is too steep or we use bad discretization, our simulations go wild due to infinite derivatives. This can be cured by integrating along the surface instead of the x-axis, but this approach will not be considered here.

A profile described by equation (7.1) is steep enough to resemble the experimental profiles but smooth enough to get good results from the simulations. Figure 7.1 shows a realization of the initial surface profile created by our simulations.

As mentioned in chapter 6, we can describe the surface profile as a Fourier series (6.1). We do the same for our new profile and calculate relaxation times τ_n for each Fourier mode in the same fashion as we did for the stream function model, section 6.1.3. The only difference is that we replace $k = 2\pi/L$ with $k_n = 2\pi n/L = kn$ in equation (6.13). Hence the new relaxation times are described by

$$\tau_n = \frac{2\eta}{\gamma k_n} \frac{\exp(2k_nH) + \exp(-2k_nH) + 2}{\exp(2k_nH) - \exp(-2k_nH) - 4k_nH}, \tag{7.2}$$

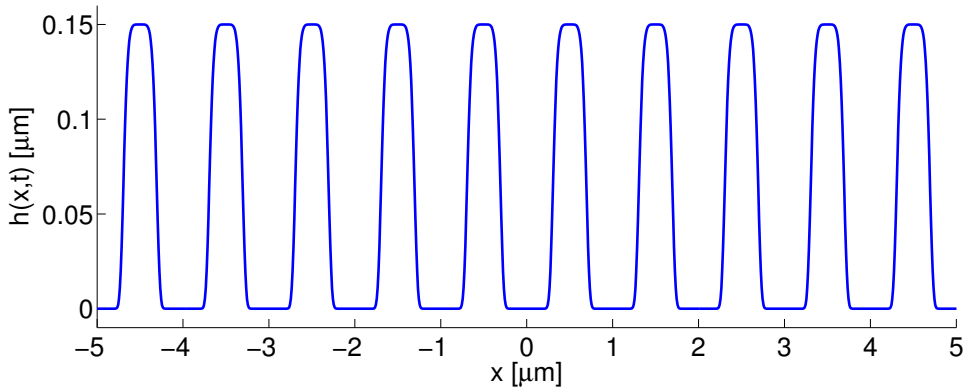

Figure 7.1: Initial surface profile given as input to the simulation. Each peak has a width of 0.4 μm and period $L = 1$ μm.

where $n = 1, 2, ...$ We recall from chapter 6 that γ denotes the surface tension, η denotes the viscosity and H denotes the mean thickness of the polymer. Furthermore, the exponential part present in equation (7.2) is effectively 1 due to $kH = 2$ for our configuration with $L = 1$ μm and $H = 2$ μm. This reduces the effective relaxation times to

$$\tau_n = \frac{2\eta}{\gamma k n} \, . \tag{7.3}$$

Now, the amplitude for each Fourier mode of the surface can be described by

$$h_n(t) = h(t = 0) \exp(-t/\tau_n) \, . \tag{7.4}$$

Evidently, the high order modes (larger n) relax much faster than the low order modes, just as expected.

Our program receives an initial surface profile with period and width determined by an input file which also contains all parameters needed to solve the electromagnetic scattering problem. These parameters are all shown in the matrix elements (4.24). Note that the surface profile $h(x, t)$ has to be at least two times differentiable. We define a surface of length $\mathcal{L}$ and discretize it into N intervals. Larger resolution (larger N) requires longer computation time. Lastly, we define an initial and final relaxation time and the number of time steps we wish to simulate. More time steps require longer computation time.

At the first time step the scattering problem is solved by the method described in chapter 4. After the first time step, we relax the surface by Fourier transforming equation (7.1) and then relaxing each mode n according to equation (7.4). While the surface is in Fourier space, we can also calculate the derivatives needed for the matrix elements (4.24) by taking advantage of the following property of the Fourier transform

$$\mathcal{F}\left[f^{(n)}(x)\right] = (ik)^n \, \mathcal{F}\left[f(x)\right] \, , \tag{7.5}$$

where $\mathcal{F}\left[f^{(n)}(x)\right]$ denotes a Fourier transform of the n-th derivative of a function $f(x)$. After taking the inverse Fourier transform of the surface, we have obtained the new relaxed surface profile. We now solve the scattering problem by the method described in chapter 4. This is repeated for every time step. We end up with a data file which

contains the mean differential reflection and transmission coefficients at each time step for each wavelength and each angle of incidence.

The simulated laser light has a finite beam width described by equation (3.17). We chose finite beam width to avoid edge-effects that arise when the beam is wider than the surface it hits. A beam width of $w = 10$ μm worked well with a $\mathcal{L} = 30$ μm long surface.

For our purpose, the reflected light is the interesting quantity. From the simulations we obtain the mean differential reflection coefficients (MDRC) as a function of scattering angle, $\theta_s^{(m)}$, where m denote the diffraction order. Since we use beams of finite width scattering on a finite sized surface, the MDRC will be distributed in a small interval, $\partial\theta_m$, around each scattering angle $\theta_s^{(m)}$. To get the reflectance from each diffraction order m, we integrate the MDRCs numerically as follows

$$R_\nu^{(m)} = \Delta\theta \sum_{\partial\theta_m} \mathrm{MDRC}\left(\theta_s^{(m)}\right) \ , \tag{7.6}$$

where $\sum_{\partial\theta_m}$ indicates a sum of elements in the interval $\partial\theta_m$. We split the whole angular axis, $-90^\circ \leq \theta \leq 90^\circ$, into cells of size $\Delta\theta = 180^\circ/j$, where j is the discretization of the angular axis. Equation (7.6) is the numerical equivalent of equation (3.27). The reflectance is proportional to intensity, hence we get intensity as a function of time for a given diffraction order m at a given viscosity η and polarization ν. We denote this intensity by I_ν^{sim}.

7.2 Optical diffraction experiment

Figure 7.2 shows an illustration of the instrumental setup of the optical diffraction experiment. A couple of photos of the experimental setup are shown in figures 7.3. The periodic structure of the polymer surface acts like a reflection grating because the period is comparable to the wavelength of the incident light [8]. An incident beam will be reflected and creates a diffraction pattern. Intensity is measured for the lowest orders of diffraction during the relaxation process. As time evolves, the surface will relax and its grating structure will decline. Still, the period L will remain constant, thus making the positions of the diffractions orders remain in place. The reflection grating equation (2.25) shows this. Both the angle of incidence and the wavelength of the laser are held constant, thus making the angles of diffraction fixed if the period does not change.

The experimental samples consist of a nanostructured layer of PMMA of mean thickness $2\,\mu$m on top of a 2 mm thick glass layer of similar dielectric function. The interface between these two layers is planar. Underneath the glass is a Ni substrate which is painted black to absorb all incident light.

At the start of the experiment, the samples are heated slowly to ensure that the temperature is distributed evenly over the whole sample. When the sample has reached the desired temperature, it is held constant at this level through the whole experiment. The intensity measurements are started as the temperature approaches this level, and are carried out until the surface is completely flat. This yields the intensity as a function of time for a given diffraction order m at a constant temperature T. We denote it I_ν^{exp}. Note that extra measures have to be taken to control the polarization in the experiments.

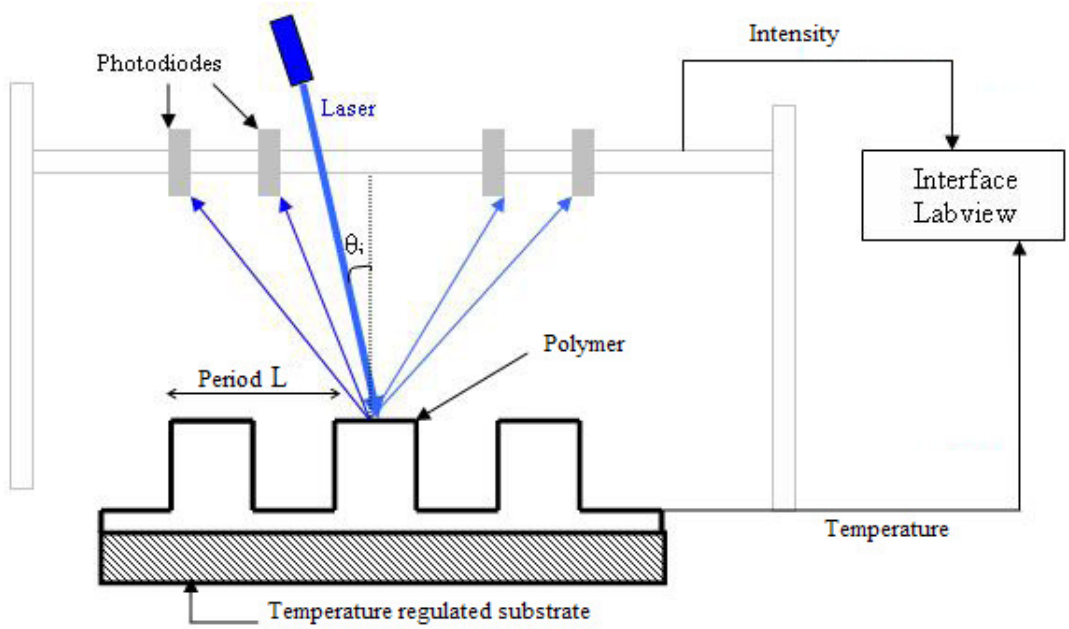

Figure 7.2: Instrumental setup of the optical diffraction experiment. A laser beam is pointed with a given angle of incidence θ_i at the periodic polymer surface. Photodiodes measure the intensity of the different diffraction orders and send the data to a computer. Temperature is controlled and measured by the same computer. The figure is taken from reference [2] and translated to English. Photos of this setup is shown in figures 7.3.

7.3 Determining $\eta(T)$

The determination of $\eta(T)$ is done by comparing the experimental data with our simulations. For each set of experimental data we do simulations to find the viscosity that corresponds to the experimentally measured temperature, *i.e.* when $I_\nu^{exp} = I_\nu^{sim}$. By repeating this process for each data set we get a set of viscosities and their corresponding temperatures, $\{\eta, T\}$. Plotting this data set yields a graph of the viscosity as a function of temperature. We call this procedure optical inversion of data.

However, the relaxation times are proportional to the viscosity, $\tau_n \sim \eta$, so strictly speaking only one set of simulation results for one η is needed. It is the time scale $t/\tau_c(\eta)$, where $\tau_c(\eta)$ is the viscosity dependent characteristic time, that matters. We define the characteristic time as the prefactor of the relaxation time, equation (7.2),

$$\tau_c(\eta) = \frac{2\eta}{\gamma k} \,. \tag{7.7}$$

Results for other viscosities can be obtained by a simple rescaling of time, *i.e.* by changing the viscosity η. Note that this only applies within the current approximation, *i.e.* the small slope approximation where $\partial_x h \ll 1$. If this approximation is not used, $\tau_n \sim \eta$ is not necessarily the case.

Even though we only need to simulate for one viscosity, there is still need for experimental results at many different temperatures to obtain $\eta(T)$.

(a) A is the laser which acts as the source for electromagnetic waves. B is where the sample is placed.

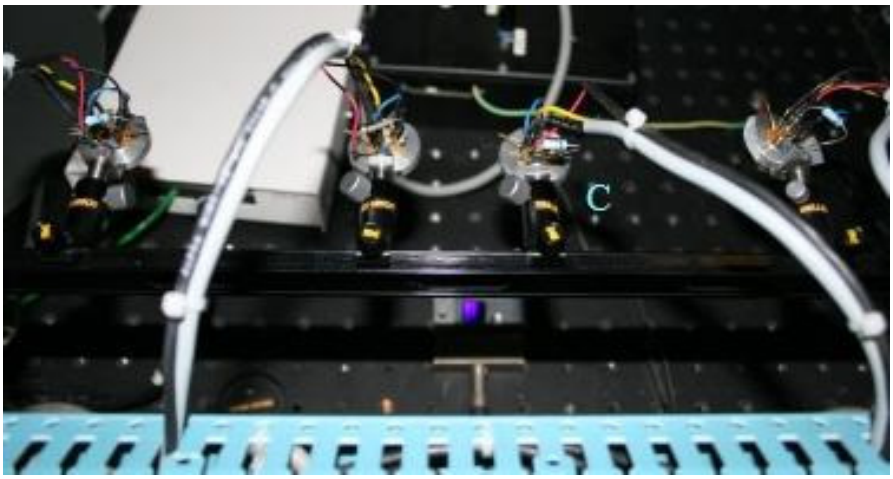

(b) C is one of the four photodiodes which measure the intensity.

Figure 7.3: Photos of the current experimental setup.

Chapter 8

Results

In this chapter, we intend to present the results obtained from simulations and experiments. The experiments were done by a group of experimentalists at Saint-Gobain Recherche, Paris. We start by showing the correspondence between the simulated relaxation and the experimental relaxation. Then we show that the relaxation is strongly dependent on the viscosity. Furthermore, we present the results obtained from the scattering simulations and compare them to the scattering experiments.

8.1 Relaxation process

Experimental data for the relaxation of the surface profiles are obtained by preparing samples as described in the introduction of this thesis and measuring the resulting surfaces using atomic force microscopy (AFM). Then the samples are heated to a temperature above the glass transition temperature, which is $T_g \approx 90°\text{C}$ for PMMA. The samples are held at a constant temperature above T_g through the entire experiment. After given relaxation times, the surfaces of the samples are again characterized with AFM. Results for the surface profile at four different times are shown in figures 8.1. We observe that as time increases, the relaxed structure becomes more and more flat. Moreover, the initial shape is not equal for each experimental sample. They are not exactly square-shaped, and there is a possibility of local differences like the spikes on top of figures 8.1(b) and 8.1(c). Also note that the vertical scale is different for each figure due to the calibration of the AFM. The experimental parameters are listed in table 8.1. These are also used in our simulations for the relaxation. Figures 8.2 show the simulated relaxation of a profile at different times and two different viscosities. These two figures show that as the viscosity is increased, the relaxation process is slower. Notice that the period of the surface remains constant during the relaxation. As we can see in

Table 8.1: Values used in the simulation of the relaxation process.

Parameter	Symbol	Value
Period	λ	1 μm
Surface tension	γ	$0.041 \cdot 10^{-3}$ J/m
Thickness of polymer film	H	2 μm
Initial height of profile	$\tilde{h}_0$	150 nm

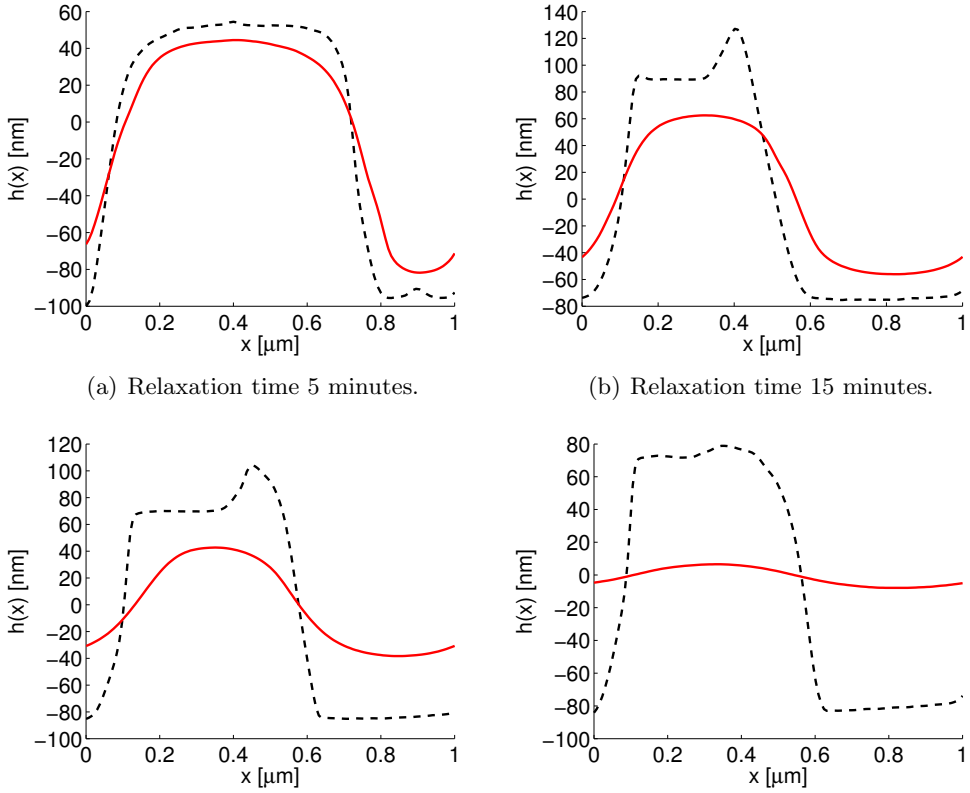

(a) Relaxation time 5 minutes.

(b) Relaxation time 15 minutes.

(c) Relaxation time 30 minutes.

(d) Relaxation time 90 minutes.

Figure 8.1: Surface profiles for different relaxation times. Black dashed lines are AFM measurements of the initial profile. Red solid lines are the experimentally obtained profiles after the noted relaxation times. Observe that as time increases, the relaxed structure flats out. The viscosities of the samples are approximately $5 \cdot 10^8$ Pa s. Note that the vertical scale is different in each figure. This is due to the calibration of the AFM.

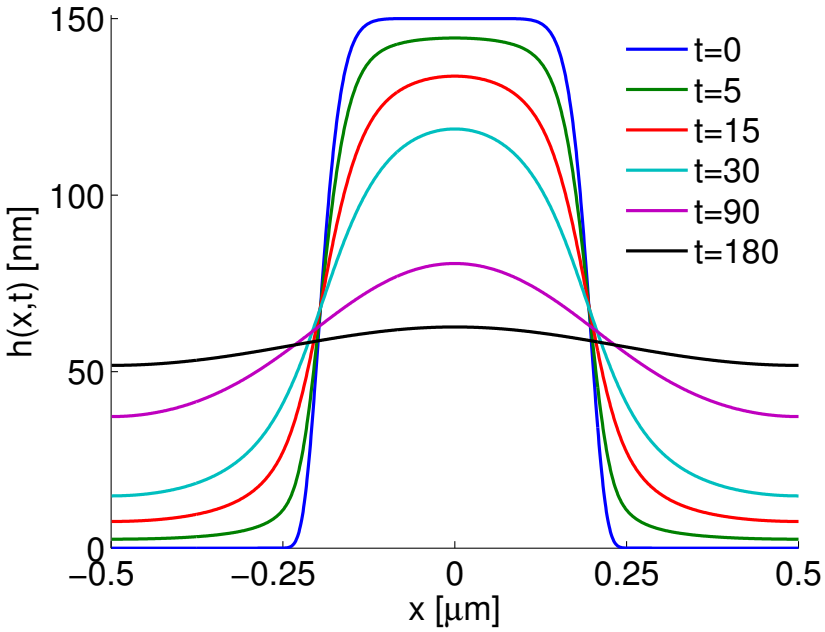

(a) Viscosity $\eta = 5 \cdot 10^8$ Pa s

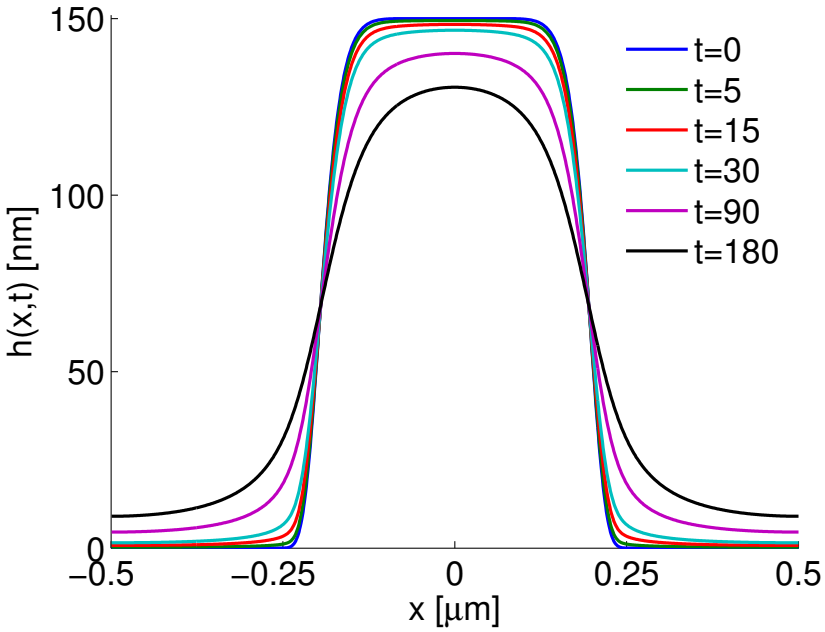

(b) Viscosity $\eta = 5 \cdot 10^9$ Pa s

Figure 8.2: Surface profiles at different times and different viscosities obtained by stream function model. The time is measured in minutes.

Table 8.2: Values used in scattering simulations.

Parameter	Value
Width of top	0.4 μm
Width of valley	0.6 μm
Period	1 μm
Angle of incidence	20°
Wavelength of laser	405 nm
Dielectric function PMMA, ϵ	2.25

figure 8.2(a), the surface evolves to an approximate sine-shape after about 30 minutes as a consequence of the fast relaxation of the high-order modes. In the end, it becomes completely flat as expected. This corresponds well with experimentally obtained AFM measurements, see figures 8.1.

8.2 Scattering simulation with one interface

In this section we show different aspects of the results obtained from rigorous computer simulations of the scattering problem. We used the numerical approach outlined in section 7.1 with input parameters as listed in table 8.2. These parameters were chosen to replicate the experimental setup. The simulations assume that the PMMA layer is infinitely thick when considering the scattering, while it is $H = 2$ μm when considering relaxation, cf. table 8.1. The reason for the different treatment is that the glass transition temperature of the glass layer is much higher than PMMA. Therefore only PMMA will relax, while glass will act as the impenetrable substrate mentioned in chapter 6. When considering scattering, glass and PMMA have very similar optical properties. Hence, we can treat H as infinite for scattering, whereas H must be the actual PMMA thickness, 2 μm, for relaxation.

Before we confront our simulation results with the experimental results, we ensure the simulations' validity by comparing them to theory. Inserting the appropriate values from table 8.2 into equations (2.15) and squaring them, we obtain the following Fresnel reflectances for s- and p-polarized light respectively

$$R_s^F = 0.0471 \ , \quad R_p^F = 0.0335 \tag{8.1}$$

The relaxation time dependent reflectances for the fundamental diffraction order, $m = 0$, are plotted in figures 8.3. The figures show that our simulations yield the Fresnel reflectances, equation (8.1), when the surface becomes flat.

Using the appropriate parameters listed in table 8.2 together with the grating equations (2.25) and (2.26) yields the number of possible diffraction orders and where these are located. We have listed the reflection diffraction orders and their angles in table 8.3 and the transmitted angles in table 8.4. The simulations yield angular distributions for s- and p-polarized light as shown in figures 8.4 and 8.5 for reflected and transmitted light respectively. The peaks of the figures are located at the same angles as the ones calculated with the grating equation, see tables 8.3 and 8.4.

In figures 8.6 we show how the reflectance in the different diffraction orders evolve in time for s- and p-polarized light, figures 8.6(a) and 8.6(b) respectively. Each figure is normalized with the Fresnel reflectance to make it easier to compare with experiments. We see that the reflectance of the fundamental diffraction order increases to the Fresnel

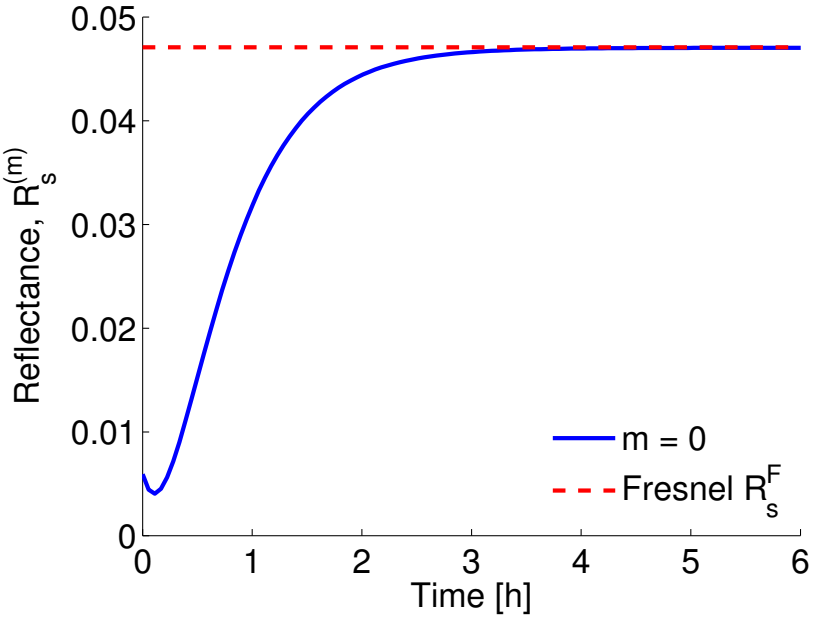

(a) s-polarized light.

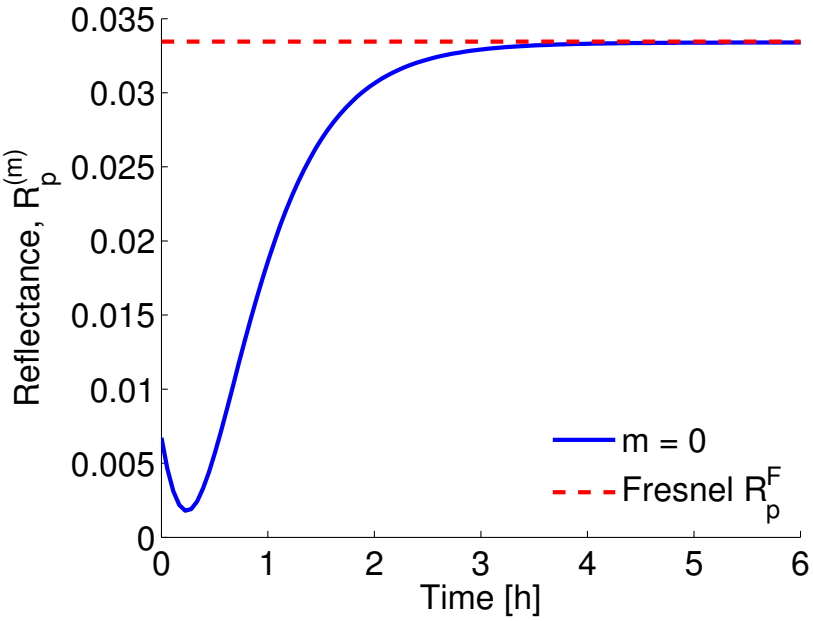

(b) p-polarized light.

Figure 8.3: The blue lines show the reflectance $R_\nu^{(m)}$ from the fundamental diffraction orders as a function of time and the red dashed lines show the theoretically calculated Fresnel reflectances R_ν^F for s- and p-polarized light, see equation (8.1). The viscosity is $\eta = 5 \cdot 10^8$ Pa s.

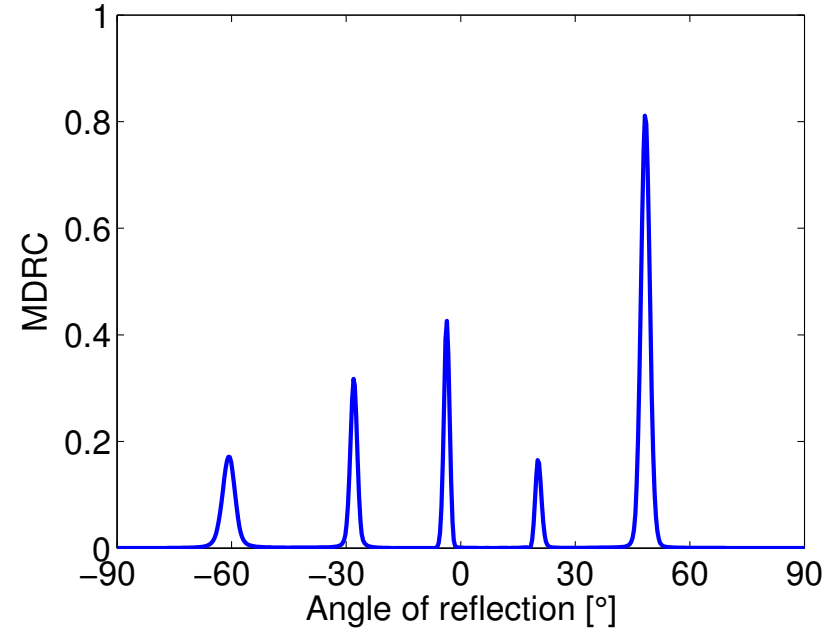

(a) s-polarized light.

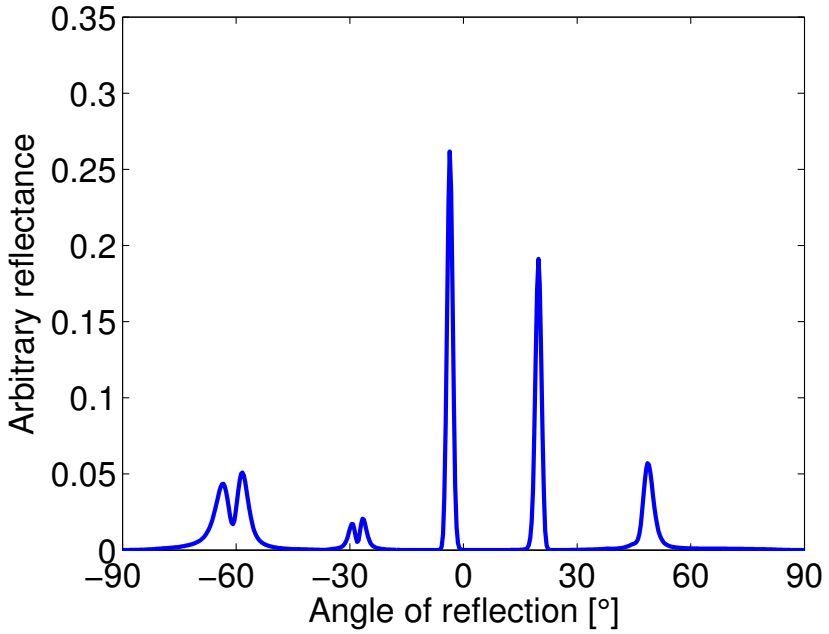

(b) p-polarized light.

Figure 8.4: Simulated angular distribution of reflected light for s- and p-polarized light before relaxation ($t = 0$).

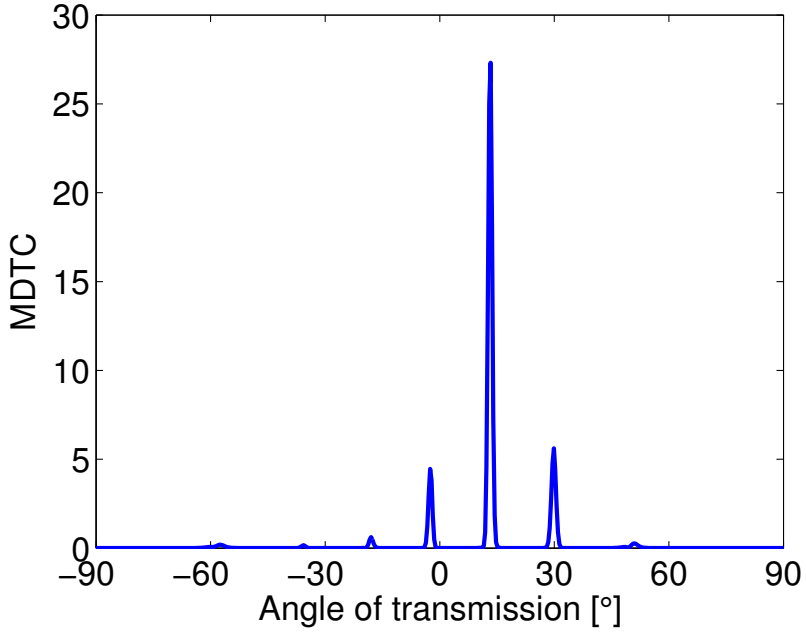

(a) s-polarized light.

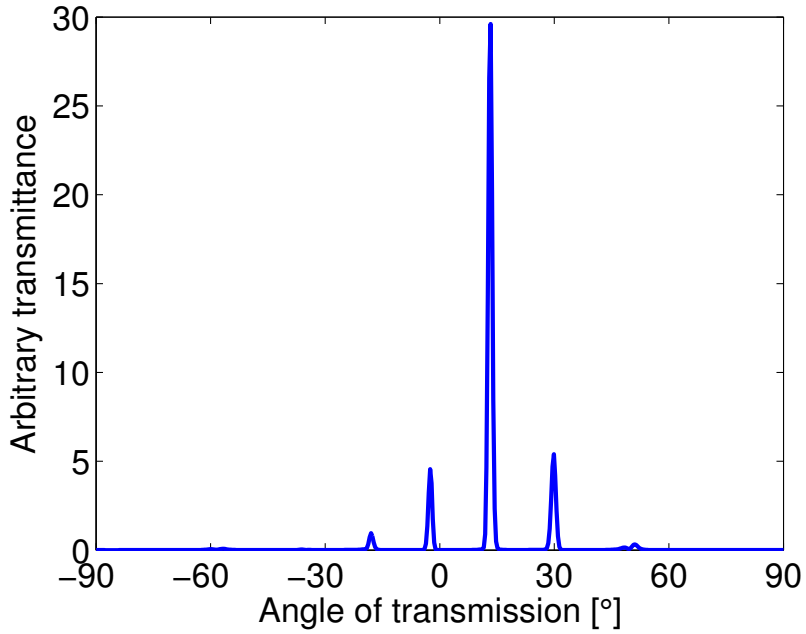

(b) p-polarized light.

Figure 8.5: Simulated angular distribution of transmitted light for s- and p-polarized light before relaxation ($t = 0$).

Table 8.3: The different reflection diffraction orders m and their theoretical angular position $\theta_s^{(m)}$. Calculated with equation (2.25).

Quantity	Value				
m	1	0	-1	-2	-3
$\theta_s^{(m)}$ [°]	48.33	20	-3.61	-27.90	-60.81

Table 8.4: The different transmission diffraction orders n and their theoretical angular position $\theta_t^{(n)}$. Calculated with equation (2.26).

Quantity	Value						
n	2	1	0	-1	-2	-3	-4
$\theta_t^{(n)}$ [°]	50.18	29.87	13.18	-2.41	-18.18	-35.59	-58.43

reflectance, while the other diffraction orders decrease and vanish when the surface becomes flat. Observe that diffraction order $m = 1$ behaves very differently for the two polarizations.

We also show experimental results in figure 8.7(a), where we have normalized with the sum of the last experimentally measured reflectances for each diffraction order, *i.e.*

$$R_{exp} = R^{(0)} + R^{(1)} + R^{(-1)} \, . \tag{8.2}$$

Since we do not have experimental data for when the surface is completely flat, we have to do it like this to get a normalization constant which resembles the Fresnel reflectance. Figure 8.7(a) shows the same behavior for the experimental data as the simulated results in figures 8.6. Even though the experimental data never reaches the Fresnel reflectance, we see that it will most likely level out to the Fresnel reflectance as it should. Ideally, we should have had better experimental data, but this is what we have and therefore we have to make do with it.

The polarization of the source used in the experiments is not known. We see from comparing figures 8.6 with figure 8.7(a) that the source is neither s- or p-polarized. Therefore we try to combine s- and p-polarized light to get a result more similar to the experimental data in figure 8.7(a). By weighting the amount of s- and p-polarized light from figures 8.6 in the following combination

$$R_u = 0.24R_s + 0.76R_p \, , \tag{8.3}$$

we get a result very similar to the experimental figure 8.7(a). Our weighted sum is shown in figure 8.7(b), where we have normalized with $R_u^F = 0.24R_s^F + 0.76R_p^F$. We observe that the weighted sum and the experimental data behaves similarly.

If the source emits light with fluctuating intensity, it might be better to look at the ratio between reflectances for the two polarizations. We define this ratio as

$$\chi_m = \frac{R_s^{(m)}}{R_p^{(m)}} \, . \tag{8.4}$$

This is plotted in figure 8.8 for viscosity $\eta = 5 \cdot 10^7$ Pa s. The figure shows that more s-polarized light is reflected than p-polarized light. We also see that after some time, when the reflectance from diffraction orders $m \neq 0$ is almost zero, the ratio starts to fluctuate

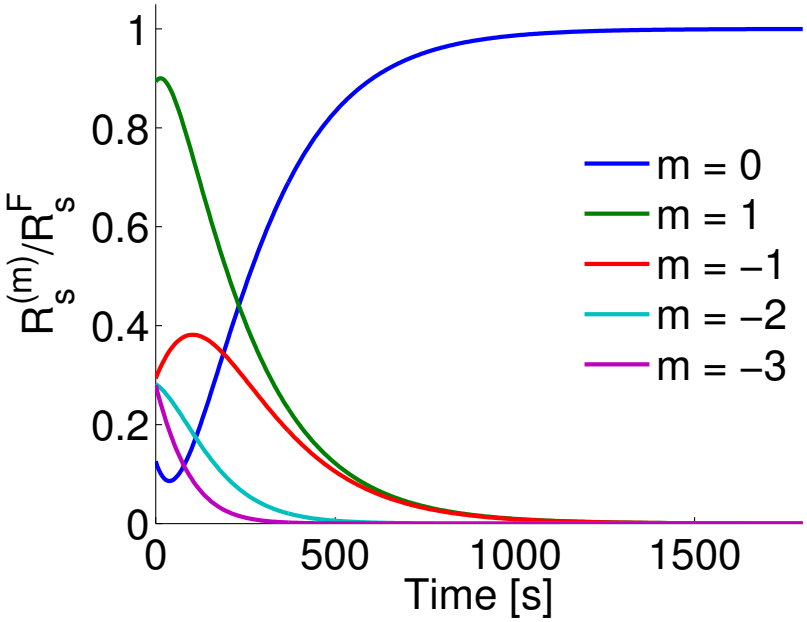

(a) s-polarized light.

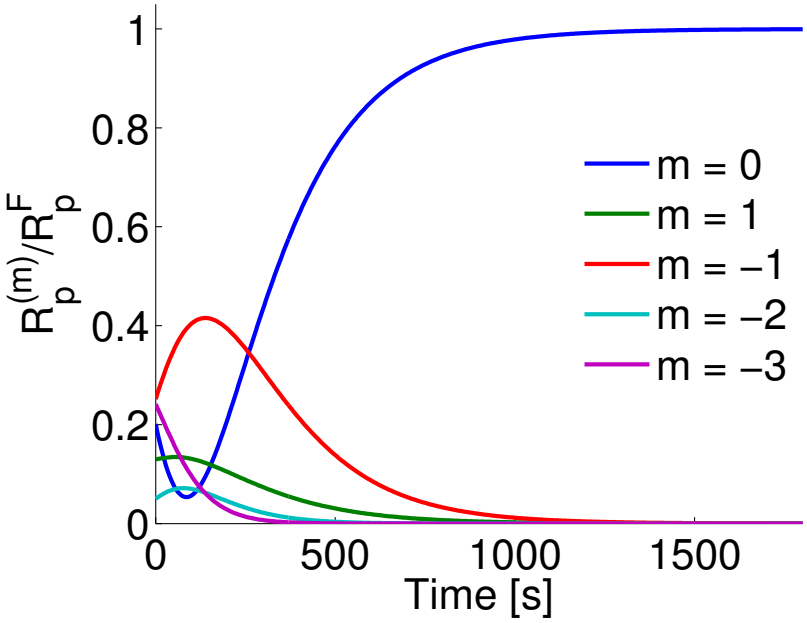

(b) p-polarized light.

Figure 8.6: Comparison of different polarizations. The figure shows the simulated reflectance, $R_\nu^{(m)}$, for each diffraction order m as a function of time. The graphs are normalized with the Fresnel reflectance, R_ν^F. The viscosity is $\eta = 5 \cdot 10^7$ Pa s.

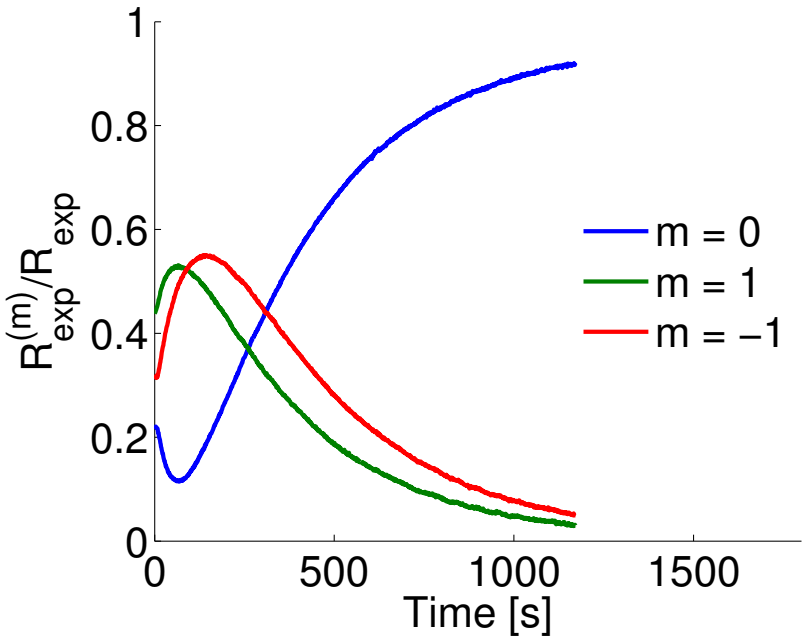

(a) Experimental data.

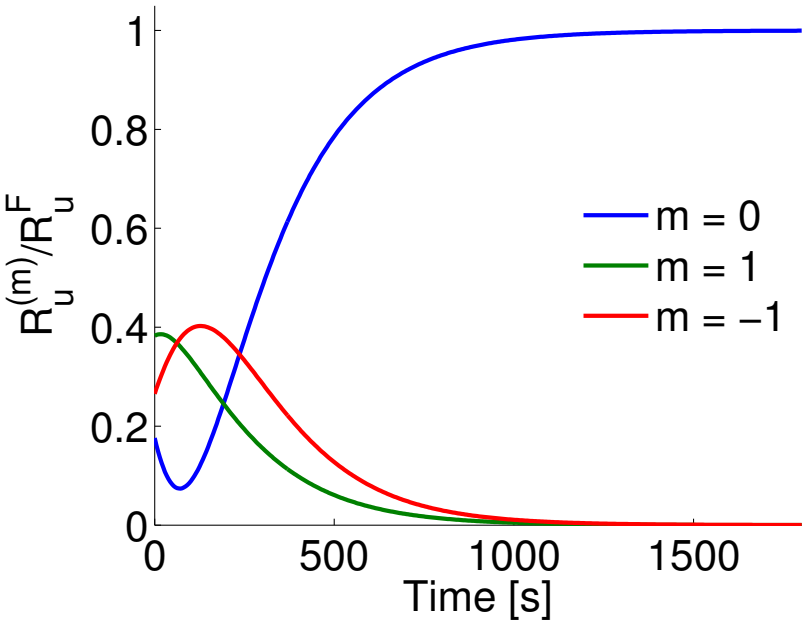

(b) Weighted sum of polarized light.

Figure 8.7: Reflectance $R_u^{(m)}$, for each diffraction order m as a function of time for the weighted sum of s– and p–polarized light, see equation (8.3). Figure (a) shows the experimental time evolution of the reflectance, $R_{exp}^{(m)}$. It is normalized with the sum of the last reflectance values, R_{exp}, defined by equation (8.2). Figure (b) is normalized with the Fresnel reflectance, R_u^F, weighted in the same manner as $R_u^{(m)}$, *i.e.* $R_u^F = 0.24R_s^F + 0.76R_p^F$. The viscosity used in this simulation is $\eta = 5 \cdot 10^7$ Pa s.

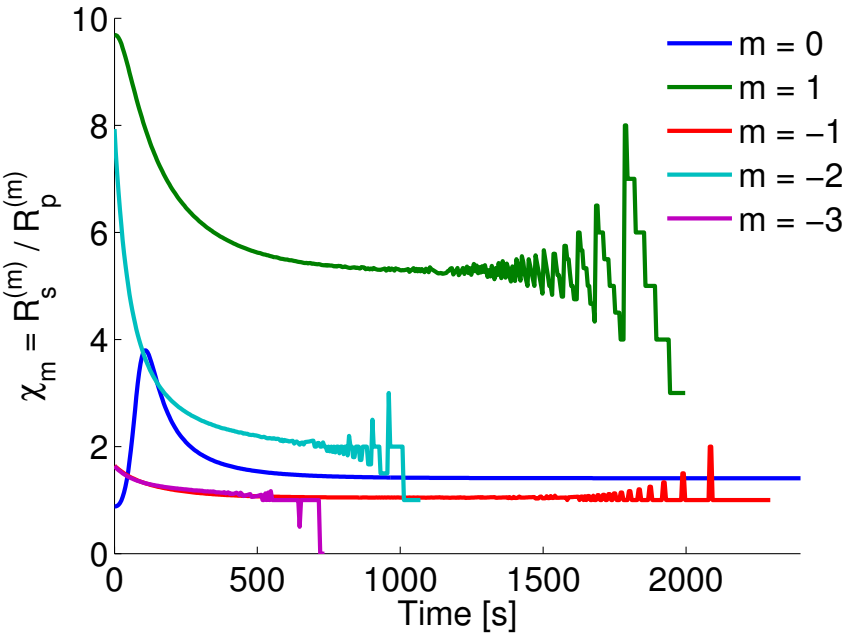

Figure 8.8: The ratio between reflectances, χ_m, as a function of time for the different diffraction orders m.

wildly. This is a numerical artifact which comes from dividing with zero. Finally, we also observe that the ratio between the fundamental diffraction orders, χ_0, is well defined for all times and contains a peak. This peak will make it easy compare simulations with experimental data.

Figures 8.9 and 8.10 show the reflectance as a function of time and viscosity at diffraction orders $m = 0, \pm 1$ for both s- and p-polarized light. As we can see, the reflectances decrease at orders $m = \pm 1$, while it increases and converges to the Fresnel reflectance R_ν^F for long times for order $m = 0$. Higher viscosities require longer time. Moreover, we observe the linear connection between relaxation time and viscosity, $\tau_n \sim \eta$, by the colors forming straight lines. This connection can also be seen in figure 8.11. It shows the ratio of the fundamental diffraction order χ_0 for viscosities $\eta = 5 \cdot 10^7$ Pa s and $\eta = 5 \cdot 10^8$ Pa s. In this figure we have plotted the ratio χ_0 versus the dimensionless time scale defined by $t/\tau_c(\eta)$, where the characteristic time $\tau_c(\eta)$ is defined in equation (7.7). We observe that the ratio is the same for both viscosities, thus also showing this linear connection between relaxation time and viscosity. Discrepancies between the two graphs are due to different time steps in the simulations, and possibly numerical noise.

To illustrate how the data inversion works, we rescale the time by $\tau_c(\eta)$ for both the experimental data from figure 8.7(a) and our weighted sum in figure 8.7(b), and plot them in the same figure. By adjusting the viscosity of the experimental time scale, we can fit the experimental data to the simulation results. Hence, we find the viscosity that corresponds to the temperature measured experimentally. Figure 8.12 shows this fitting. Here, $\eta(103°\text{C}) = 6 \cdot 10^7$ Pa s. Note that the experimental samples might not be perfectly periodic, and there might be local differences from sample to sample. After some relaxation, these local differences should be gone. As a consequence, comparing the long term behavior of the reflectances will probably be better than comparing at early times.

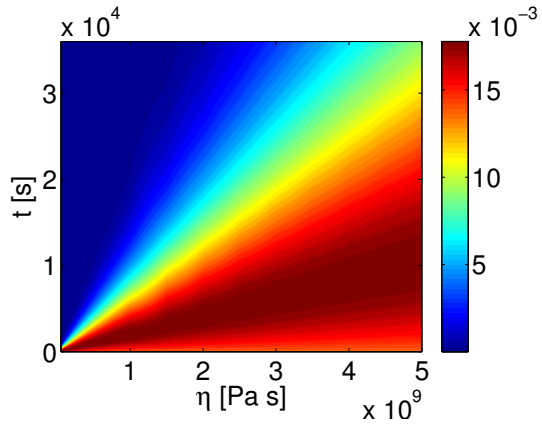

(a) $m = -1$

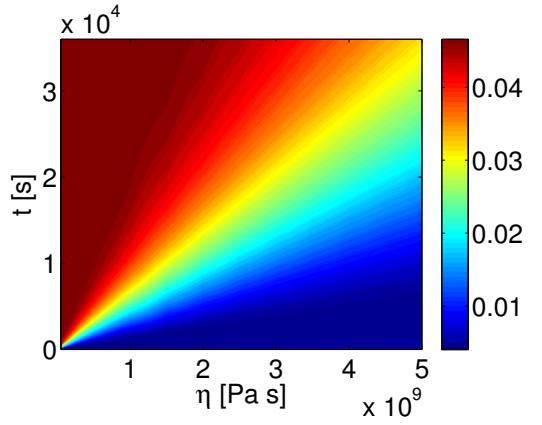

(b) $m = 0$

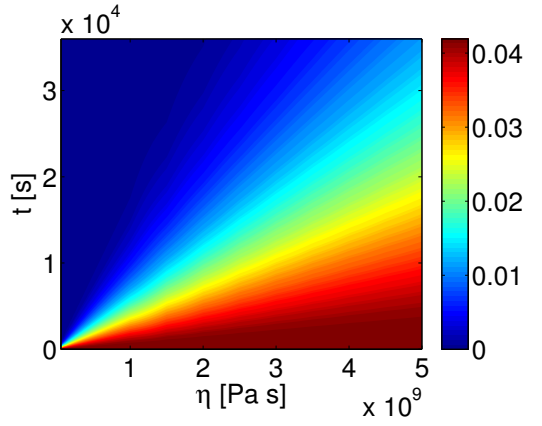

(c) $m = 1$

Figure 8.9: Reflectance $R_s^{(m)}$ as a function of time for different viscosities. Figures show diffraction orders $m = 0$ and $m = \pm 1$ for s-polarized light. The color bars show the reflectance, $R_s^{(m)}$. We observe that the fundamental diffraction order increases while the other two decreases.

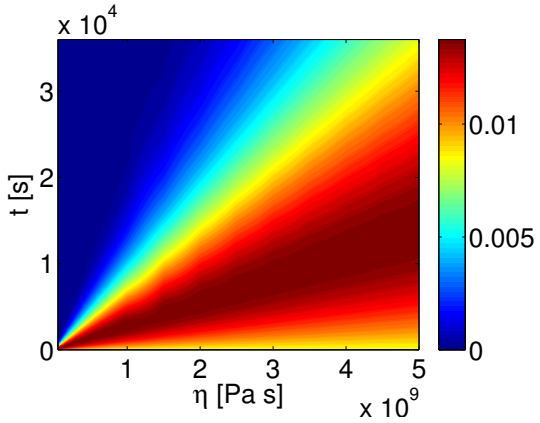

(a) $m = -1$

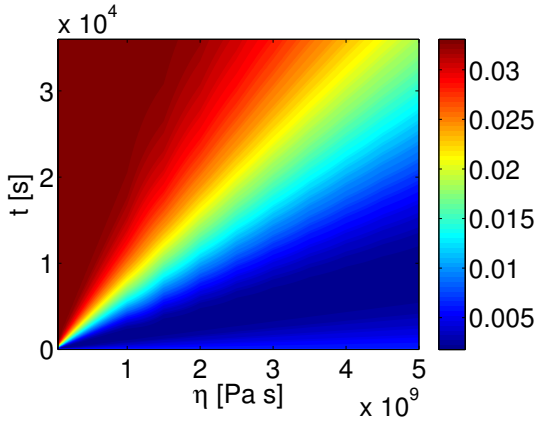

(b) $m = 0$

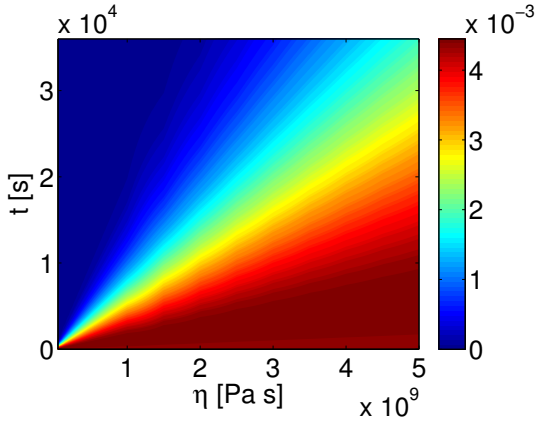

(c) $m = 1$

Figure 8.10: Reflectance $R_p^{(m)}$as a function of time for different viscosities. Figures show diffraction orders $m = 0$ and $m = \pm 1$ for p-polarized light. The color bars show the reflectance, $R_p^{(m)}$. We observe that the fundamental diffraction order increases while the other two decreases.

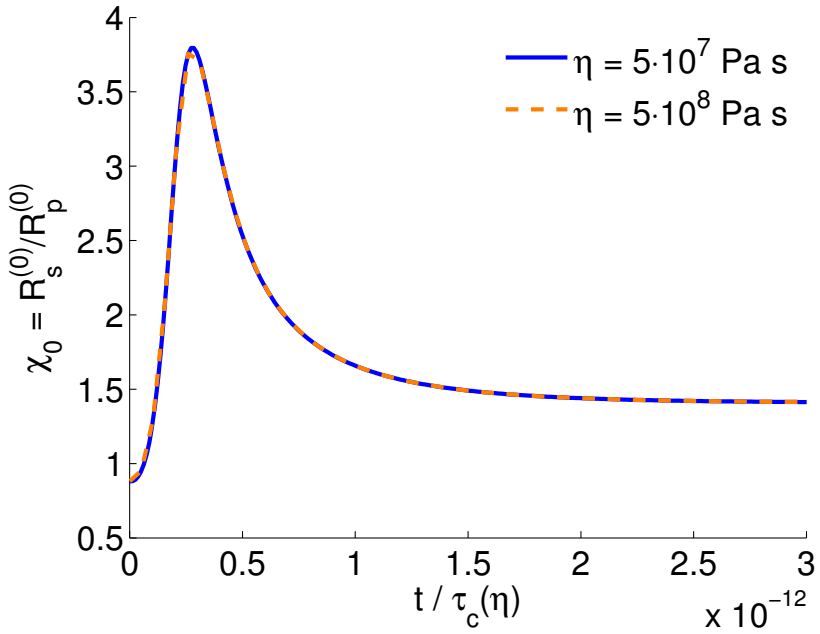

Figure 8.11: The ratio χ_0 as a function of dimensionless time. The characteristic time $\tau_c(\eta)$ is different for the two viscosities, η. See figure legend for the values of η.

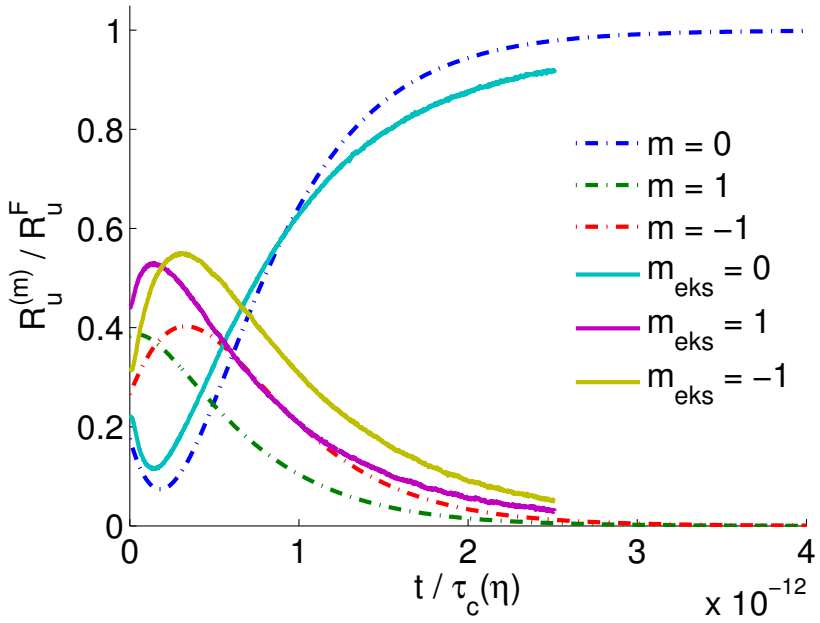

Figure 8.12: Normalized reflectance as a function of dimensionless time. Solid lines show experimental data and dash dotted lines show our simulation results. We have rescaled the time with the characteristic time. The viscosity for the simulation results is $\eta = 5 \cdot 10^7$ Pa s, while the experimental data is fitted with a viscosity of $\eta = 6 \cdot 10^7$ Pa s.

Table 8.5: Theoretically calculated Fresnel reflectances.

Polarization, ν	$\Delta\epsilon$	One layer	Two layers	Difference, ΔR_ν^F
	+5%	0.0525	0.0530	0.0095
s	0	0.0471	0.0471	0
	−5%	0.0416	0.0420	0.0096
	+5%	0.0376	0.0380	0.0105
p	0	0.0335	0.0335	0
	−5%	0.0293	0.0296	0.0102

Table 8.6: Simulated Fresnel reflectances.

Polarization, ν	$\Delta\epsilon$	One layer	Two layers	Difference, ΔR_ν^F
	+5%	0.0526	0.0537	0.0209
s	0	0.0471	0.0453	−0.0382
	−5%	0.0417	0.0380	−0.0887
	+5%	0.0376	0.0348	−0.0745
p	0	0.0334	0.0351	0.0509
	−5%	0.0293	0.0252	−0.1399

8.3 Scattering simulation with two interfaces

As mentioned in section 7.2, the experimental samples consist of a structured PMMA layer on top of a glass layer. We thought it would be interesting to examine effects that may arise when there is a mismatch between the dielectric functions of glass and PMMA. Therefore we ran simulations with the glass layer included and varied the dielectric functions of PMMA. Figures 8.13 show the reflectance evolution for the fundamental diffraction order for both polarizations where we have a 2 μm thick layer of PMMA on top of glass with similar dielectric function[3]. The reflectance is compared with the Fresnel reflectance calculated for only one layer of PMMA and no glass, see equation (8.1). We see that the reflectance differs when we vary the dielectric function. Note that when $\Delta\epsilon = 0$, *i.e.* the equivalent of one layer, the two layer Fresnel reflectance differs from the one layer Fresnel reflectance. This should not happen.

All results here are obtained by using the same parameters as listed in table 8.2. The other diffraction orders behave just as shown for the no glass case shown in figures 8.6 with different numerical values. Therefore we chose to not include figures for them here.

We use equation (3.33) to calculate the Fresnel reflectances for a two layer sample where we vary the dielectric function of PMMA with ±5%. We define the variation of the PMMA dielectric function as $\Delta\epsilon$. Tables 8.5 and 8.6 show reflectances, theoretical and simulated respectively, for one- and two-layer samples where $\Delta\epsilon = 0, \pm 5\%$.

Figures 8.14 show the difference between the two and one layer Fresnel reflectances for both polarizations. The dielectric function of the glass layer is held constant at $\epsilon_{glass} = 2.25$, while the dielectric function of the PMMA layer is varied. We define the difference by

$$\Delta R_\nu^F = \frac{R_\nu^{(m)}(2) - R_\nu^{(m)}(1)}{R_\nu^{(m)}(1)} \,, \tag{8.5}$$

[3]Note that the symbol for the dielectric function in the figures is slightly different from the current notation. They denote the same quantity, *i.e.* $\varepsilon \equiv \epsilon$.

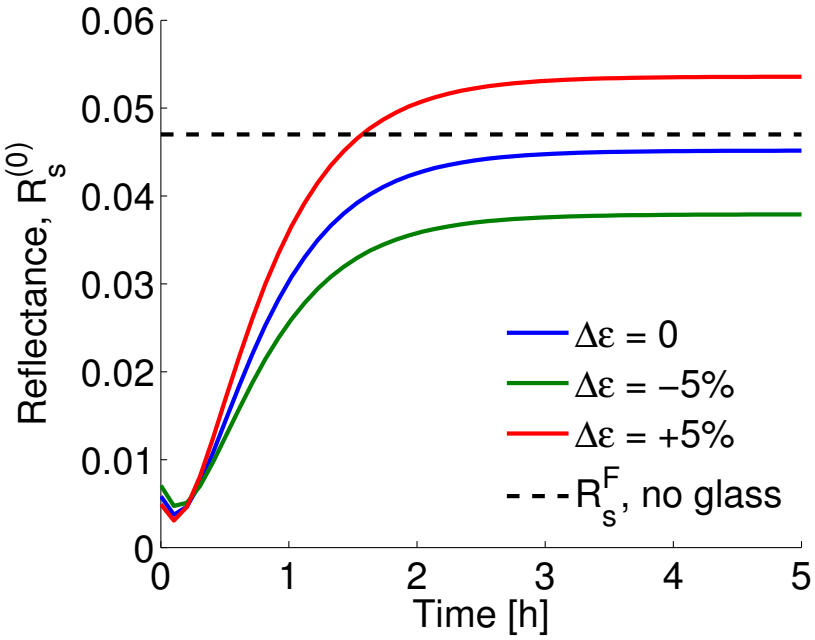

(a) s-polarized light.

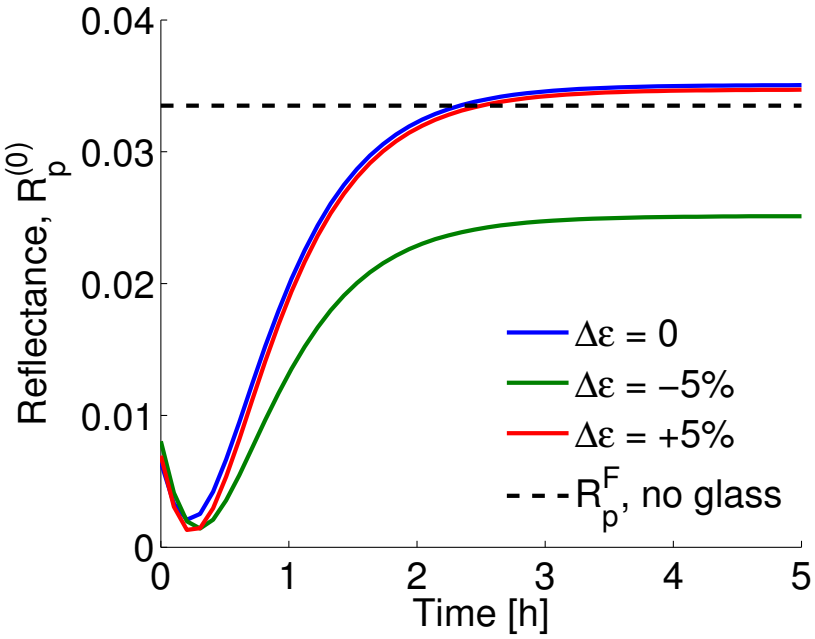

(b) p-polarized light.

Figure 8.13: Reflectance as a function of time for the fundamental diffraction order $R_\nu^{(0)}$ at different PMMA dielectric functions for both polarizations, ν. The dashed black lines show the Fresnel reflectance R_ν^F for the case where there is no glass and $\Delta\epsilon = 0$. The cause of the sharp edges for the reflectances at early times is few time steps.

where $R_\nu^{(m)}(1)$ and $R_\nu^{(m)}(2)$ denote the Fresnel reflectance for polarization ν and diffraction order m from one and two layers respectively. From table 8.5 and figure 8.14 we observe that theoretically, there is just a very small difference in reflectance when including a second layer of similar dielectric function. Therefore, we can use one layer simulations without compromising our results.

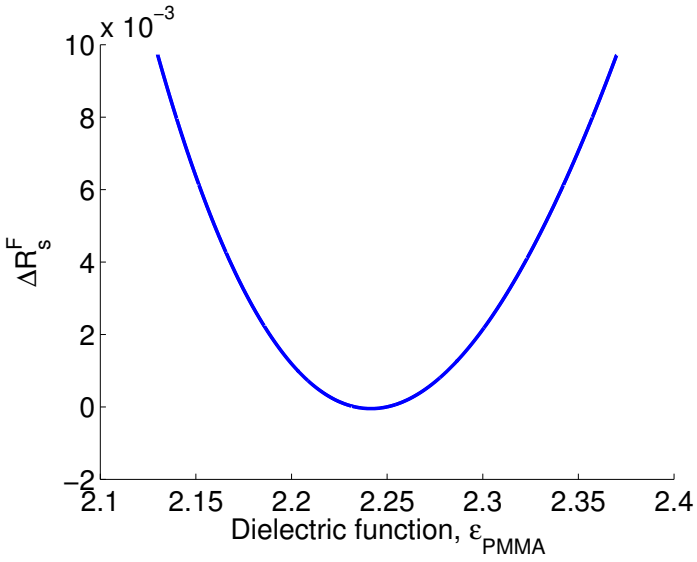

(a) s-polarized light.

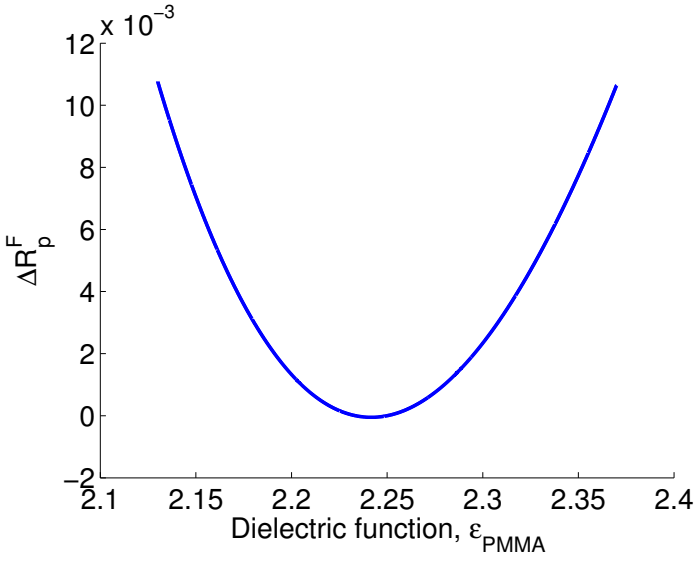

(b) p-polarized light.

Figure 8.14: The change in Fresnel reflectance ΔR_ν^F as a function of dielectric function of PMMA, ϵ_{PMMA}, when we include a glass layer underneath the PMMA. ϵ_{glass} is held constant at 2.25. The change is defined by equation (8.5).

Chapter 9

Discussion

In this chapter we discuss the results presented in the previous chapter. We have divided this chapter into sections just like the results chapter. Finally we include a section where we discuss future work and improvements.

9.1 Relaxation process

The initial shape of the samples to be used in the relaxation experiments is a square-wave, where the slope becomes infinite ($\partial_x h = \infty$) at periodical intervals, see figure 1.1. As mentioned in chapter 6 and 7, a square-wave can be described by a Fourier series, equation (6.1). The higher order modes of this series are needed to describe the sharp corners, while the lower order modes are the foundation of the profile. The lowest order mode is just a simple sine-function of a period equal to that of the initial profile. All higher order modes have smaller periods than the lowest order mode. Equation (7.2) shows that the higher the order, the faster it relaxes, *i.e.* larger k_n yield smaller relaxation time, τ_n. Thus, we expect that the experimental profiles converge asymptotically to a sine-shape with the period of the fundamental mode during the relaxation process. Figures 8.1 show AFM measurements of experimental samples. We observe that the surface gradually becomes sine-shaped, thus confirming our expectation. Moreover, figure 8.2(a) shows that our model for the relaxation also behaves accordingly. Note that the period stays constant, thus making the diffraction orders stay in the same location through the entire relaxation in accordance with the grating equations (2.25) and (2.26).

Studying figures 8.1 reveals that the initial profiles of the experimental samples are not exactly square-shaped. This discrepancy may be caused by the problems with imprinting discussed in the introduction, or by the AFM readings. The steep slopes of the samples make it difficult to obtain accurate measurements by AFM due to tip effects. In addition, the experimental samples have local differences, like the small spikes at the top in figures 8.1(b) and 8.1(c). We observe that after a short period of relaxation the local peaks are gone and that the experimental samples' shape corresponds to the ones obtained from our stream function model in figures 8.2. This indicates that the uncertainty of the surface profiles is much larger at early times than at later stages of relaxation. Hence, we might not need a more accurate model for the relaxation at early times due to experimental limitations.

Figures 8.2 show that the higher order modes relax faster than the low order modes thus making the profile more smooth. These figures also describe the strong viscosity-

dependency for the relaxation times. After three hours a profile of viscosity $\eta = 5 \cdot 10^8$ Pa s is almost completely flat, see figure 8.2(a), while a profile of viscosity $\eta = 5 \cdot 10^9$ Pa s is far from flat, see figure 8.2(b). The similar behavior between our model and the experiments, figures 8.2(a) and 8.1 respectively, in addition to the strong viscosity dependence of the relaxation presented in figures 8.2, indicate that our simple stream function model describes the general behavior of relaxation quite well.

Note that to get the relaxation times τ_n, we have assumed the small slope approximation $\partial_x h \ll 1$ for each mode even though the total surface is steep $\partial_x h \gg 1$. Nevertheless, we assume that this is ok since our simulations show both qualitative and quantitative similarities to the experiments. Hence, our model for relaxation is well suited for the optical diffraction simulations.

There is also an issue with the experimental setup worth mentioning. There is no way of knowing for sure if the temperature distribution really is uniform within the polymer film. Inhomogeneous temperature distribution may give rise to different relaxations at different positions in the sample due to energy transport caused by temperature gradients. Note that we have here assumed that these effects are small and therefore negligible.

Temperature is probably the quantity which is most difficult to control experimentally in our case, and therefore gives rise to high uncertainty. One improvement could be to encase the sample in a glass box covered with some thin opaque material. Covering the box with some fabric, removes diffusely scattered light from the glass box. The laser light will propagate through the fabric without being attenuated due to the fabric's small thickness. By keeping the temperature inside this box relatively high, the heat transport from PMMA to air will be reduced. This way we can hopefully obtain a more uniform temperature distribution within the sample during the experiment.

9.2 Scattering simulation with one interface

The first results presented in section 8.2 show that our simulations correspond well with theory. This is necessary to ensure the validity of our simulations. Scattering from a flat surface without absorption will give the Fresnel reflectance calculated from the appropriate Fresnel's equation (2.17a). As we can see from figures 8.3, the simulated fundamental order reflectances from the surface converge with the Fresnel reflectances, equations (8.1) for our setup, when the surface becomes flat.

Furthermore, we expect that the reflectance from the other diffraction orders will decrease as time evolves and the interface between air and PMMA becomes planar. Examination of figures 8.6 show that these reflectances diminish when the surface becomes flat. Hence, the behavior of the reflectances at large times is correct. An interesting feature is that the reflectance from the fundamental diffraction order decreases before it starts to increase to the Fresnel reflectance. It could be interesting to find what causes this "dip".

Moreover, the diffraction orders should be located at the same angles as the ones we calculated from the grating equations (2.25) and (2.26). Comparing figures 8.4 and 8.5 with tables 8.3 and 8.4 show that both the reflected and transmitted diffraction orders from our simulations appear at the correct positions according to theory.

The cause of the splitting of the $m = -2$ and $m = -3$ peaks in figure 8.4(b) for p-polarized light is unknown. It does not come from the sharp edges at early relaxation times, because it persists through the entire relaxation process. This also excludes mul-

tiple scattering effects which might cause destructive interference. Multiple scattering is when the light is scattered on the surface more than one time before it leaves the vicinity of the surface. The question remains unanswered.

Another test for the accuracy of our simulations is the unitarity, equation (3.28). If this quantity differs significantly from one, we know that some energy is lost in the simulation, for instance by absorption. When there is no absorption in the system, a unitarity much different from one indicates that the simulation is most likely wrong. The reason for this can be some numerical artifact coming from poorly chosen discretization or system properties, or it might be some physical effect like multiple scattering.

Multiple scattering will very likely happen when our surface is in its early stages of relaxation. We observe this by looking at the unitarity from our simulations. At the early stages, when the surface has sharp edges and is quite rough, the unitarity lies below one. Still, the values are above 0.9 for p-polarized light and above 0.94 for s-polarized light, which is good enough, especially since the unitarity increases quickly to one as the surface gradually smoothens. Hence, our simulations conserve energy after a short period of time.

When we take the uncertainty of the experimental samples' early shape into consideration, we realize that the unitarity problem at early times does not matter. No matter how close the unitarity is to one, we cannot get accurate results at early stages when we compare experimental data with simulation results due to the experimental uncertainty. After a short period of relaxation the uncertainty of the samples' shape is much smaller and the unitarity is approximately one. Taking the correct behavior of the reflectances and the correct positioning of the diffraction orders into account, we conclude that our simulations are valid for all times except at the earliest stages of relaxation.

We can probably improve the unitarity by better discretization, which requires more computer memory than we have had at our disposal. Changing the way we discretize the surface from along the x-axis to along the actual surface might yield better unitarity.

The width of the diffraction orders is caused by the finite width of the incoming laser beam and the finite length of the surface. If we used a plane wave and infinite length surface, the angular distribution figures 8.4 and 8.5 would have had δ-function spikes at the calculated angles. Due to numerical limitations it is impossible to simulate this system, therefore we used the finite width beam impinging onto a finite width surface. As stated before, a finite width beam represents the laser quite well and a finite size surface corresponds to the finite sized experimental samples. To get the correct reflectance, we integrate the MDRCs according to equation (7.6) for each diffraction order over an interval around the calculated angles listed in table 8.3, to make reflectance versus time-plots like figures 8.6 show.

Figures 8.6 indicate polarization dependent behavior of the different diffraction orders m. For instance, order $m = 1$ for s-polarized light is dominant at early times, while $m = 1$ for p-polarized light has a quite low reflectance. To compare the experimental results with simulation results, the time evolution of the reflectances should be similar. Hence, it is important to know the polarization of the laser used in the experiments. We also see the different behavior between the diffraction orders of both polarizations in figure 8.8. It is clearly shown that the reflectance of s-polarized light is larger than p-polarized light. The reason for the oscillations for orders $m \neq 0$ is that the reflectances $R_\nu^{(m)}$ are approximately zero due to the relaxing surface. We observe that the ratio of the fundamental diffraction order χ_0 behaves nicely, which it should because $R_\nu^{(m)}$ is always finite.

Figure 8.7(a) is made from preliminary experimental data where neither the temperature or the polarization is controlled very well. By adjusting the fractions of s- and p-polarized light we found a combination, see equation (8.3), that reproduces the qualitative behavior of the experimental data for diffraction orders $m = 0, \pm 1$. Comparing figure 8.7(a) and figure 8.7(b) we see the similar behavior. The mismatch in the numerical values for normalized reflectance is due to the normalization. If we had experimental data for longer times, *i.e.* when the surface is relaxed and completely flat, we could have normalized with the correct normalization constant which corresponds to the Fresnel reflectance. As we can see from figure 8.7(a), the reflectance from the fundamental diffraction order is still increasing, therefore we get the wrong normalization constant when normalizing with the last value as this does not correspond to the Fresnel reflectance. The reason for the normalization is that the experiments do not measure absolute intensity. Therefore, we have to normalize to compare experiments with simulation.

Inspection of figures 8.9 and 8.10 shows how the reflectance evolves in time for different viscosities. As expected, we see that higher viscosity results in longer relaxation times and thus the reflectance changes more slowly. Moreover, we see that the relaxation time is linearly dependent on viscosity from the colors forming straight lines. We stated in section 7.3 that it is the time scale that matters. Figure 8.11 shows the ratio χ_0 for two different viscosities as a function of the dimensionless time scale $t/\tau_c(\eta)$, where the characteristic relaxation time $\tau_c(\eta)$ is defined in equation (7.7). We observe that the ratio for both viscosities coincide. Hence, one simulation with a given set of parameters should suffice to determine the time-evolution of the reflectance regardless of viscosity. If we wish to look at the behavior of another viscosity, we only need to change η in the characteristic time $\tau_c(\eta)$ to obtain the correct time-evolution for this viscosity. Again, note that this only applies in the small slope approximation. Without this approximation, the linear dependence between the relaxation time and the viscosity is not necessarily the case. The dimensional analysis in section 6.2 strengthens the linear connection between the relaxation time and the viscosity, but as mentioned, we cannot fully exclude other possibilities like $\tau \sim \eta \exp(\eta/A)$.

Even though we only have one incomplete set of experimental data, there are clearly similarities to be seen between the experiment and the simulations, figures 8.7(a) and 8.7(b) respectively. The behavior in time and the values for the reflectance for all the orders are very similar. Figure 8.12 shows a way to determine the temperature dependent viscosity. The time scale of the simulation result is rescaled with the characteristic time for the viscosity used in the simulation, $\eta = 5 \cdot 10^7$ Pa s. Then we rescale the time scale of the experimental data with similar characteristic time. By adjusting the viscosity used for the experimental characteristic time, we try to fit the experimental reflectances to the simulated reflectances. The viscosity which gives best fit is most likely the viscosity of PMMA at the measured temperature.

Here, the viscosity at the measured temperature $T = 103°\text{C}$ is $\eta = 6 \cdot 10^7$ Pa s, though it is probably not correct since we do not know the polarization of the source and because the reflectance never reaches the Fresnel reflectance. We used the sum of the last reflectance value of each diffraction order from the experimental data to get an approximate Fresnel reflectance, R^F. Better experimental results and knowledge of polarization is needed to use this method. Still, figure 8.12 illustrates how the method works and it shows promising results.

The rescaling of time by the characteristic relaxation time $\tau_c(\eta)$ can be done for all figures showing reflectance as a function of time. We have chosen to show most of these

figures without rescaling to give the reader a view of the times that are characteristic for the relaxation process.

Placing a polarization switching device in front of the laser makes us able to measure the intensity of both polarizations, I_ν, at approximately the same time. The ratio between intensities is proportional to the ratio between reflectances. By comparing χ_0 the fundamental diffraction order, shown in figure 8.11, with the ratio of the experimentally obtained intensities, I_s/I_p, we can find the viscosity that corresponds to the measured temperature. Since the ratio χ_0 has only one peak, it is easy to fit it to experimental data by adjusting the viscosity of the characteristic relaxation time which we use to rescale the time. We also have to compare with the other diffraction orders $m \neq 0$ too, but by first comparing with the fundamental order gives a good indication to whether we are close or not. This method is equivalent to the method proposed a earlier in this section, but might be better suited for determining $\eta(T)$ if the intensity from the source fluctuates in time. The ratio between the two polarizations should be the same regardless of intensity. We assume that the intensity fluctuations are much slower than the polarization switching device such that the measurements of R_s and R_p are done at the same intensity.

9.3 Scattering simulation with two interfaces

As the experimental samples consist of a structured PMMA layer on top of glass of similar dielectric function, we include the glass in our simulations to see how the glass layer will affect the simulations. The reflectance from the fundamental order is reduced for s-polarized light while it is increased for p-polarized light, see figure 8.13. Something must be wrong with our simulations. Even if the experimental results are preliminary, they do not deviate much from the simulations done without the glass layer, see figures 8.6, 8.7 and 8.12.

Theoretically, the inclusion of the glass layer with dielectric function close to the dielectric function of PMMA should not affect the reflectance the way it is shown in figure 8.13. Figures 8.14 show that the change in reflectance ΔR_ν^F between one layer and two layers with almost equal dielectric function is very small. Comparing the theoretically calculated one layer reflectances from table 8.5 with the simulated ones in table 8.6 shows that theory and simulation correspond very well. When comparing the two layer reflectances we see big differences that should not be there. Even when $\epsilon_{PMMA} = \epsilon_{glass}$, which is the equivalent of having just one layer, there is a difference which should not be there.

The angular distribution for the diffraction orders from the two layer simulations is the same as for the distribution from the one layer simulations shown in figures 8.4 and 8.5. Hence, this is not the problem. Furthermore, the unitarity evolves just like for the one layer simulations, so this is not the problem either. When including an extra layer, the simulation requires much more memory. Still, we had enough memory to use the same discretization and system size as for the one layer simulations. One possible reason for the strange behavior might be that we get a singular set of equations when the dielectric function is equal at both sides of the interface. Anyhow, for the time being we should dismiss the two layer simulations.

Fortunately, we only need one layer simulations to determine the viscosity. Figures 8.14 show that the theoretical difference between one and two layers with similar dielectric functions is negligible, *i.e.* $\Delta R_\nu^F < 0.01$. PMMA and the glass used in the

experiments have almost equal dielectric functions and therefore the glass will not affect the reflectances noticeably. Moreover, when we compare experiments with our one layer simulations, we see that the behavior is very similar, see figures 8.7. Hence, we can still determine the viscosity even though our program halts when including the glass layer. The difficulties with controlling temperature and energy transport within the relaxing samples will most likely affect the measurements much more than the mismatch in dielectric functions.

9.4 Future work

Basically, the only thing that remains is to obtain many sets of experimental data for different temperatures and fitting them to the simulation result. Before we can do this, we have to ensure that the experimental data is usable. First, we need to control the polarization of the source, either by measuring the polarization or by applying a polarization switching device in front of the source, as mentioned in the previous section. We also need to control temperature to ensure the same relaxation at all positions in the sample. The box solution proposed is a possible way of improving this.

Lastly, the experimentalists should do some experiments where they check if there is a noticeable difference between one or more layers of equal and slightly different dielectric function. They should also find which interface that contributes the most to the reflectance. Is it the air/PMMA-, PMMA/glass or glass/substrate-interface? This can easily be checked by doing experiments with completely flat surfaces. In doing this, it is also easy to compare with theory as the measured reflectance should be equal to the Fresnel reflectance.

As soon as this is done, we are ready to determine the viscosity as a function of temperature by the method proposed in this thesis.

One of the questions that remains unanswered is the cause of the "dip" in the reflectance from the fundamental diffraction order at early times. This "dip" also appears in the experimental results, so it is not a numerical artifact. Another question is the split of the $m = -2$ and $m = -3$ peaks for p-polarized light.

Finally, it would be interesting to find the cause of the weird behavior of the simulations when including more than one layer.

Chapter 10

Conclusion

The main purpose of this thesis was to study scattering of polarized light from a relaxing periodic nanostructured highly viscous surface. This is one of the steps in developing a new indirect method of determining the viscosity as a function of temperature for a polymer material. By comparing scattering simulations where the viscosity is known with scattering experiments where the temperature is held constant, we can find the temperature dependent viscosity by data inversion.

We have studied the fundamental electromagnetic equations and rederived a method to solve the scattering problem by rigorous numerical simulations. Applying our simple model for relaxation to higher orders of the Fourier expansion of the surface profile and implementing it in the scattering program, enabled us to simulate scattering from a relaxing surface. Our simulation results was confronted with theory to ensure the validity of the numerical approach, and then compared to preliminary experimental data.

The simulations indicate that there are differences between the behavior of the two polarizations, which means that polarization control is important when doing the experiments. Furthermore, we have discovered that the numerical method used here yield strange results when we include several layers. Fortunately, simulations with only one layer still give results that corresponds nicely with experimental results.

We also find that we only need one simulation due to the linear connection between relaxation time and viscosity. With just a simple rescaling of time, we are able to fit experimental data to the simulation results. Hence, the data inversion will require much less time than if we had to run simulations for each viscosity. Taking the preliminary experimental results into consideration, we see that this method shows promising results. With more experimental results we would have been able to determine the viscosity as a function of temperature.

Bibliography

[1] S. Y. Chou, P. R. Krauss, and P. J. Renstrom. *Imprint of sub-25 nm vias and trenches in polymers. Appl. Phys. Lett.*, 67:3114–3116, 1995.

[2] A. Revaux. *Rhéologie de films structurés par nanoimpression.* Master's thesis, Laboratoire Surface du Verre et Interfaces, UMR 125, CNRS/Saint-Gobain, Paris, 2008.

[3] K. Norrman, A. Ghanbari-Siahkali, and N. B. Larsen. *Studies of spin-coated polymer films. Annu. Rep. Prog. Chem., Sect. C: Phys. Chem.*, 101:174–201, 2005.

[4] Wikipedia. Nanolithography imprinting. Article dated 11. December 2008, *http://en.wikipedia.org/Nanoimprint_lithography.*

[5] Y. Hirai, T. Yoshikawa, N. Takagi, and S. Yoshiba. *Mechanical Properties of Polymethyl methacrylate(PMMA) for Nano Imprint Lithography. Journal of Photopolymer Science and Technology*, 16:615–620, 2003.

[6] J. D. Jackson. *Classical Electrodynamics.* John Wiley & Sons, Inc, 2^{nd} edition, 1975.

[7] D. J. Griffiths. *Introduction to Electrodynamics.* Prentice-Hall International, Inc., 1999.

[8] F. L. Pedrotti, L. S. Pedrotti, and L. M. Pedrotti. *Introduction to Optics.* Pearson Education, Inc., 3^{rd} edition, 2007.

[9] C. Kittel. *Introduction to Solid State Physics.* John Wiley & Sons, Inc, 8^{th} edition, 2005.

[10] I. Simonsen. *A random walk through rough surface scattering phenomena.* arXiv:cond-mat/0408017v1, 2004.

[11] R. A. Adams. *Calculus – A Complete Course.* Pearson Education Inc., 5^{th} edition, 2003.

[12] A. A. Maradudin, T. Michel, A. R. McGurn, and E. R. Mendez. *Enhanced Backscattering of Light from a Random Grating. Ann. Phys*, 203:255–307, 1990.

[13] M. Born and E. Wolf. *Principles of Optics.* Pergamon Press, 6^{th} edition, 1980.

[14] A. Sommerfeld. *Optik*. Akademische Verlagsgesellschaft Geest & Portig K.-G, 2^{nd} edition, 1959.

[15] M. Abramowitz and I. A. Stegun. *Handbook of Mathematical Functions*. Dover, New York, 1964.

[16] W. H. Press, S. A. Teukolsky, W. T. Vetterling, and B. P. Flannery. *Numerical Recipes*. Cambridge University Press, 3^{rd} edition, 2007.

[17] L. D. Landau and E. M. Lifschitz. *Fluid Mechanics*. Pergamon Press, 1^{st} edition, 1966.

[18] A. Oron, S. H. Davis, and S. G. Bankoff. *Long-scale evolution of thin liquid films*. *Rev. Mod. Phys*, 69:931–978, 1997.

[19] F. M. White. *Fluid Mechanics*. Pearson Education, Inc., 5^{th} edition, 2003.

[20] E. Guyon, J. P. Hulin, L. Petit, and C. D. Mitescu. *Physical Hydrodynamics*. Oxford University Press, 2001.

[21] J. A. Ogilvy. *Theory of Wave Scattering From Random Rough Surfaces*. Taylor & Francis, 1991.

[22] E. Kreyszig. *Advanced Engineering Mathematics*. John Wiley & Sons, Inc., 1999.